REVIEW

National Science Open
5: 20260014, 2026
https://doi.org/10.1360/nso/20260014

Materials Science

Special Topic: Hollow Multishelled Structure

Hollow multishelled structure: A versatile platform for boosting the performance of sodium-ion batteries

Zhifan Song[1,2], Jiangyan Wang[2,4,*], Na Wang[1,*], Dan Wang[2,3,*] & Ranbo Yu[1,3,*]

[1]*School of Metallurgical and Ecological Engineering, University of Science and Technology Beijing, Beijing 100083, China;*
[2]*State Key Laboratory of Biopharmaceutical Preparation and Delivery, Institute of Process Engineering, Chinese Academy of Sciences, Beijing 100190, China;*
[3]*State Key Laboratory of Intelligent Construction and Healthy Operation and Maintenance of Deep Underground Engineering, College of Chemistry and Environmental Engineering, Shenzhen University, Shenzhen 518071, China;*
[4]*School of Chemical Engineering, University of Chinese Academy of Sciences, Beijing 100049, China*

*Corresponding authors (emails: jywang@ipe.ac.cn (Jiangyan Wang); nawang@ustb.edu.cn (Na Wang); danwang@szu.edu.cn (Dan Wang); ranboyu@szu.edu.cn (Ranbo Yu))

Received 27 January 2026; Revised 9 March 2026; Accepted 19 March 2026; Published online 20 March 2026

Abstract: Sodium-ion batteries (SIBs), with abundant resources and low cost, have established themselves as a core candidate for large-scale energy storage in the post-lithium-ion battery (LIB) era. However, electrode materials suffer from severe volume expansion, sluggish ion transport kinetics, and low energy density due to the larger radius and higher atomic weight of sodium. These challenges cannot be resolved by simply replicating LIB technologies and have thus become the core technical barriers hindering the industrialization of SIBs. Endowed with hierarchical shells, internal cavities, a large accessible surface area to volume ratio, and excellent loading capacity, the hollow multishelled structure (HoMS) effectively alleviates these issues. This review systematically summarizes the design strategies and optimization mechanisms of HoMS for SIB anodes (carbon-based, alloy-type, and conversion-type materials) and cathodes (metal oxides, polyanionic compounds (PCs), and Prussian blue analogues (PBAs)), focusing on addressing key performance degradation bottlenecks. It also outlines synthesis challenges and industrialization prospects, expanding SIB electrode structural portfolios and offering actionable guidance for rational HoMS-based electrode design.

Keywords: hollow multishelled structure (HoMS), sodium-ion battery, anode, cathode, optimization mechanism

INTRODUCTION

The rapid development of advanced energy materials and devices is driving an urgent demand for energy storage technologies with higher efficiency and lower cost. Lithium-ion batteries (LIBs) have been extensively implemented in electric vehicles and portable electronic products, which fully demonstrates their superiority in high energy density and long cycle life [1,2]. However, the sustainable development of LIBs is limited by the scarcity and uneven geographical distribution of lithium resources [3]. Sodium-ion batteries (SIBs) have emerged as one of the most promising alternatives and thus garnered tremendous research attention. This is primarily attributed to their similar working mechanism to LIBs, coupled with the abundant

and widespread sodium resources, which align with the requirements of large-scale production and cost-effective development [4–7]. Moreover, SIBs exhibit superior low-temperature performance and intrinsic safety, maintaining considerable charge/discharge efficiency and cycling performance even under extreme conditions [8–10]. Notably, despite the larger ionic size of Na^+, its Stokes diameter is smaller than that of Li^+. Theoretically, the electrolyte with the same concentration delivers higher ionic conductivity than lithium salt-based electrolytes, which is beneficial for realizing outstanding rate capability [8,11].

Nevertheless, SIBs still suffer from several critical bottlenecks that must be addressed for practical applications. First, the larger ionic radius of Na^+ induces a pronounced volume variation of electrode materials during charge/discharge cycles [12]. This structural degradation over long-term cycling leads to rapid capacity fading and low energy density. Second, the intrinsically sluggish diffusion kinetics of Na^+ within electrode materials imposes a fundamental limitation on the fast-charging capability of SIBs [13]. Additionally, inadequate electronic conductivity of electrode materials restricts interfacial charge transfer kinetics, which further deteriorates the overall electrochemical performance, especially the fast-charging ability at low temperatures [14,15]. These scientific issues arising from the characteristics of Na^+ are considerably more serious than those in LIB systems, thus necessitating more decisive strategies. To overcome these issues, extensive efforts have been reported in the rational design of electrode materials [16–18], optimization of electrolyte formulations [19,20], and modification of separators [21,22], as well as the device assembly process. Among various structural engineering strategies, the hollow multishelled structure (HoMS) has shown enormous potential in tackling these challenges of SIBs because of its unique structural merits.

HoMS represents a category of three-dimensional (3D) hollow architectures, which is constructed by the ordered arrangement of multiple shells and internal cavities, and has been demonstrated as a highly attractive platform for energy storage [23–26]. When integrated into SIBs, HoMS can translate its unique structural merits into targeted solutions for inherent shortcomings of SIBs, which are distinct from its roles in LIBs. For instance, the intrinsic cavities between adjacent shells can serve as buffer space to accommodate the ultra-large volume expansion occurring during charge/discharge cycles, thereby enhancing the structural stability of electrode materials [27,28]. Moreover, the hierarchical multishelled configuration shortens both ionic and electronic transport pathways, promoting charge transfer efficiency and enabling competitive rate capability [29,30]. In addition, rational tuning of shell thickness and cavity volume can endow the materials with a large specific surface area, which not only enlarges the electrode/electrolyte contact area, but also exposes more active sites to facilitate the rapid intercalation and deintercalation of Na^+ [31–33]. Therefore, continuous research and innovation of HoMS in SIB applications are expected to boost the overall sodium storage performance among a series of modifications and optimization strategies.

Herein, we focus on how HoMS engineering can address the key bottlenecks of SIBs, clarifying the essential differences from the application of HoMS in LIBs. First, we briefly outline the major challenges of SIBs as well as the critical scientific issues that impede their sustainable practical applications. Then, centering on the design of HoMS in electrode materials, we elaborate on the underlying mechanisms by which HoMS optimizes the electrochemical performance of SIBs, including alleviating volume expansion, enhancing ion/electron transport efficiency, and optimizing interface contact. Finally, on the basis of summarizing the design rules of HoMS, we highlight the challenges confronted in structural design and provide a perspective on the future development of HoMS for next-generation SIB optimization. This review furnishes

significant theoretical and practical guidance for the design and application of HoMS in SIBs, and is particularly crucial for breaking through the technical bottlenecks of SIBs and promoting their large-scale commercialization.

CHALLENGES OF SIBS

With analogous working mechanisms and great potential for cost-effective development, SIBs were investigated alongside LIBs in the early stage [34]. However, owing to the higher electrochemical potential and lighter atomic weight of Li, LIBs have consistently outperformed SIBs in terms of energy density, which led to the neglect of SIB research for a long time [35,36]. Although the past few years have witnessed burgeoning research efforts on Na chemistry and the continuous enhancement of their performance, significant challenges still impede their extensive commercialization. Both the development of various electrode material systems and full-cell performance require in-depth attention. Energy density has long been recognized as one of the pivotal performance metrics for SIBs. During the intercalation and deintercalation of Na^+, the structural changes and stresses generated will lead to the structural instability of electrode materials. More critically, excessive volume expansion will lead to pulverization and detachment of electrode materials, resulting in increased internal resistance and compromised interfacial stability between the electrode and electrolyte [37–39]. All these issues are detrimental to the cycle life of the battery devices. Consequently, constrained by the inferior ionic diffusion kinetics and the large ionic size of Na^+, the entire SIB system suffers from relatively low energy density and poor cycling stability [40]. Hard carbon, for instance, as one of the most promising anode materials, also faces the problem of unstable solid electrolyte interphase (SEI) formation [41]. The irreversible side reactions and unstable SEI layer during the initial charge/discharge cycle will restrict the improvement of initial Coulombic efficiency (ICE) [42]. In addition, the consumption of limited Na resources on the cathode side will simultaneously result in lower energy density [43]. Fast-charging capability, a key feature for electric vehicles, requires excellent sodium storage kinetics. Nevertheless, Na^+ diffusion within the lattice is subject to substantial resistance. Meanwhile, the insufficient electronic conductivity further limits the rapid charge transfer, ultimately failing to meet the requirements of fast-charging and high-power output applications [44]. Therefore, it is necessary to improve the diffusion kinetics of Na^+ in both electrode materials and electrolytes to enhance fast-charging performance, thereby enabling high-power applications. Although analogous issues also arise in LIBs, they are far more pronounced in SIB systems. This is mainly attributed to the larger ionic radius of Na^+, which leads to slower kinetics, more severe volume variation, and less stable interfaces during the intercalation/deintercalation processes. To address these challenges, HoMS design typically serves as an auxiliary and complementary optimization strategy in LIBs, whereas it can directly determine the feasibility of the entire SIB systems. Briefly, high-performance SIBs present more rigorous requirements for HoMS design in ion/electron transport efficiency, structural stability, and interfacial stabilization, which renders the corresponding optimization more specific and irreplaceable relative to LIB systems.

As illustrated in Figure 1, the rational design of HoMS provides an effective strategy to address these challenges. The buffer effect of internal cavities mitigates stress concentration and prevents structural collapse of the materials, thus exhibiting excellent cycling stability [45]. Compared with a single-shelled

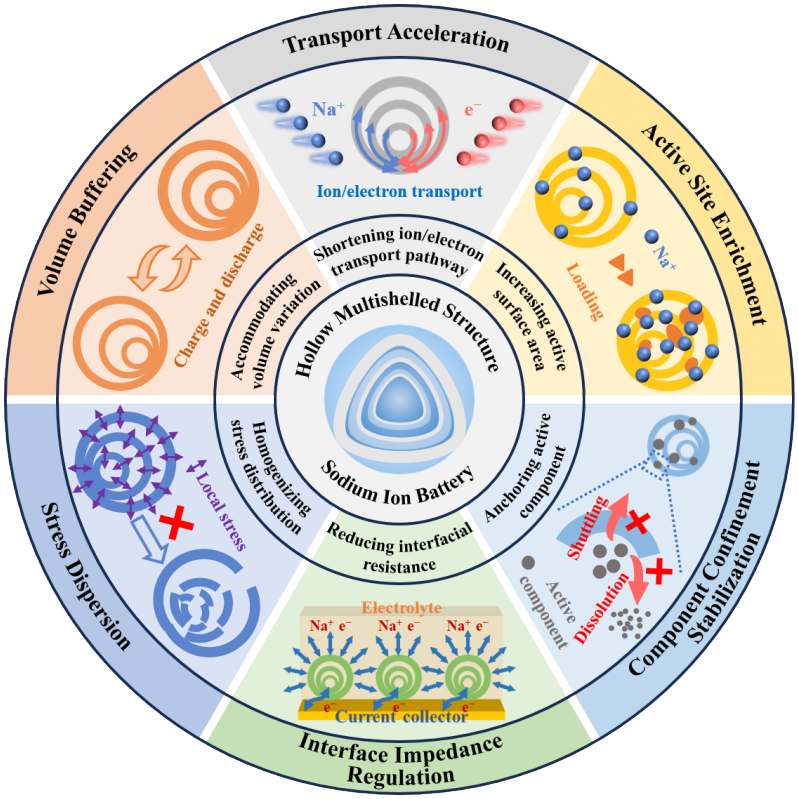

Figure 1 Schematic diagram showing the critical merits of HoMS for overcoming the challenges of SIBs.

hollow structure, HoMS eliminates redundant cavities while realizing multiple buffering effects, and enables the accommodation of more active materials, which effectively boosts the energy density of SIBs. Another advantage of HoMS is the hierarchical surface that endows a markedly elevated specific surface area, furnishing abundant active sites for sodium storage and rapid reaction kinetics [46]. Furthermore, compared with conventional porous nanomaterials, the interaction between shells shortens the ion and electron transport pathways, ensuring fast sodium storage kinetics, as Na^+ can diffuse rapidly through the intershell channels with reduced diffusion resistance [47]. More importantly, HoMS allows precise regulation of shell number, pore size, shell composition, and surface properties, achieving multifunctional synergy and multidimensional structural modulation, which distinguishes it from simple hollow structures and porous materials. For example, the reported double-shelled hollow carbon@WS_2 benefits from its porous and multishelled structure, creating favorable conditions for increasing the electrochemically active surface area, thus guaranteeing rapid charge transfer and Na^+ diffusion [48].

Although both anode and cathode materials suffer from similar issues, the underlying mechanism and emphasis of HoMS engineering differ owing to the intrinsic distinctions in their sodium storage mechanisms and critical challenges. For anode materials (e.g., FeS_2, SnO_2), the sodium storage process typically involves conversion or alloying reactions accompanied by severe volume expansion. Accordingly, the design of HoMS focuses more on reserving sufficient interior voids or providing a structural support to alleviate volume expansion. For some materials with low electronic conductivity, carbon coating or heterostructure engineering on the shell surface is often required to improve conductivity and suppress the dissolution and

shuttling of intermediate products such as polysulfides. For cathode materials, the sodium storage mechanism is dominated by Na^+ intercalation/deintercalation with relatively small volume variation, but they suffer from transition metal dissolution, surface side reactions, and structural degradation at high voltages. Therefore, the design of HoMS for cathodes emphasizes enhanced rate capability by shortening ion diffusion pathways, as well as stabilizing the cathode/electrolyte interface and suppressing transition metal dissolution and side reactions. Consequently, systematic investigation of HoMS engineering is of great significance for breaking through the technical bottlenecks of SIBs and achieving high-performance metrics that meet the demands of practical applications.

HOMS FOR ANODE OPTIMIZATION

As one of the pivotal components of SIBs, anode materials directly determine the energy density, power density, and cycle life of the devices [49,50]. Currently, research on SIB anode materials is mainly focused on carbon materials [51–53], alloy-type materials [54–57], transition metal compounds [58–62], and other emerging materials [63,64]. To meet the requirements of high-performance SIBs, these materials are expected to possess appropriate Na^+ intercalation potential, high specific capacity, superior ion/electron conductivity, and excellent structural stability. However, in practical applications, each category of these materials exhibits inherent limitations. For instance, the low theoretical specific capacity of carbon materials restricts the enhancement of energy density [65], while alloy-type materials suffer from severe volume expansion during cycling [55], which leads to poor cycling stability. Therefore, rational optimization of anode materials is essential to fabricate high-performance SIBs.

HoMS offers a versatile "shell-cavity" platform to address the aforementioned drawbacks. Both the precise parameter design of shells and cavities and the regulation of the physical and chemical states of active materials enable the accurate modulation of the electrochemical performance of anode materials. In the following sections, the optimization strategies and underlying mechanisms of HoMS for different types of anode materials will be elaborated.

Carbon-based HoMS

To date, various carbon materials, such as hard carbon [53], soft carbon [66], graphene [67], and graphdiyne [68], have been extensively explored for various electrochemical energy storage devices. Among them, hard carbon is unanimously regarded as the most technologically relevant anode for SIBs, owing to the superior industrial maturity, the largest application scale, and the most essential role [69,70]. Endowed with abundant reserves, cost-effectiveness, and facile derivation from various biomass precursors, hard carbon delivers satisfactory cycling stability and moderate theoretical specific capacity. Nevertheless, its intrinsically limited capacity and relatively low ICE require further optimization for practical full-cell configurations [43].

The fabrication and application of carbon-based HoMS (C-HoMS) offer an effective strategy to address these challenges. C-HoMS with tunable structural parameters can be rationally constructed via template-assisted methods, self-assembly approaches, and other synthetic strategies. As illustrated in Figure 2A, single-shelled hollow carbon spheres can be obtained by polymerizing phenolic resin on the surface of SiO_2

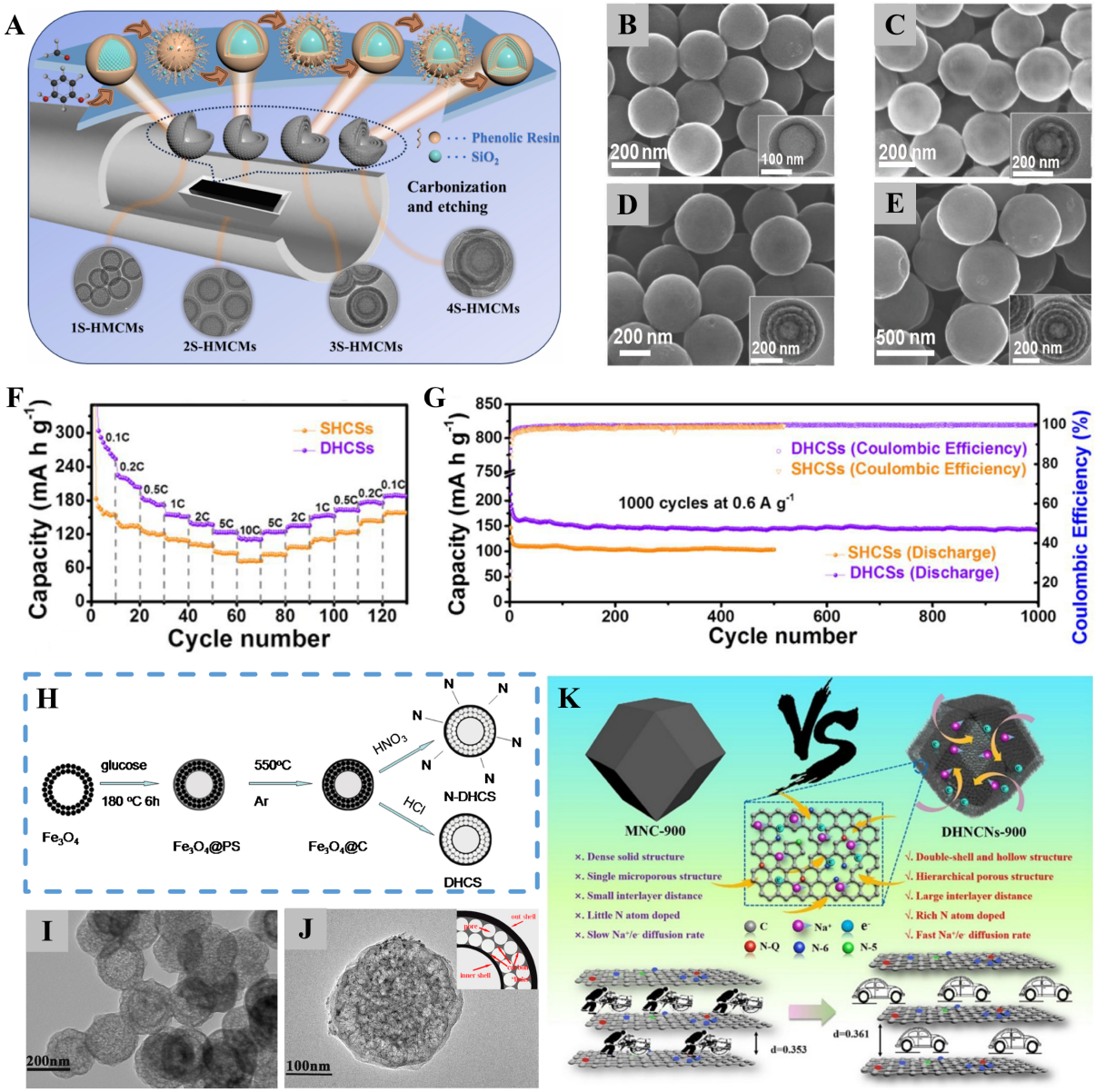

Figure 2 (A) Schematic diagram of the synthesis process of MS-HMCMs. Reproduced with permission from Ref. [71]. Copyright©2024, Elsevier Ltd. SEM images of (B) single-shelled HCNs (1S-HCNs), (C) double-shelled HCNs (2S-HCNs), (D) three-shelled HCNs (3S-HCNs), and (E) four-shelled HCNs (4S-HCNs), respectively. The insets are their TEM images. Reproduced with permission from Ref. [72]. Copyright©2018, Wiley‐VCH Verlag GmbH & Co. KGaA, Weinheim. (F) Rate capabilities of SHCS and DHCS electrodes. (G) Cycle performance of SHCS and DHCS electrodes under 0.6 A g^{-1}. (F, G) Reproduced with permission from Ref. [73]. Copyright©2020, Elsevier Ltd. (H) Schematic of the synthesis steps for DHCSs and N-DHCSs. (I) High-magnification TEM image of the as-obtained N-DHCSs. (J) Low-magnification high-resolution TEM (HRTEM) image of the as-obtained N-DHCSs and simulated pattern inset. (H–J) Reproduced with permission from Ref. [74]. Copyright©2015, Elsevier Ltd. (K) Schematic illustration for the unique feature of DHNCNs-900 as anode material in SIBs. Reproduced with permission from Ref. [75]. Copyright©2024, Elsevier Ltd.

hard templates, followed by carbonization and subsequent template etching [71]. On this basis, well-defined double-, triple-, and quadruple-shelled hollow carbon spheres (MS-HMCMs) can also be fabricated through multi-step templating and sequential polymerization processes. In the application of hard carbon for SIBs, the structural superiority of multishelled architectures is not only reflected in accommodating the large volume

strain during charge/discharge cycles, but also in the fact that the overall electrochemical performance is highly dependent on the precise parameters of the multishelled configurations. Bin *et al*. [72] adopted a similar method to prepare hard carbon nanospheres with different shell numbers, as presented in Figure 2B–E. With the increase in shell number, the authors found that the enhancement of overall capacity was attributed to the contribution from the plateau region rather than the sloping region. This is because the high specific surface area provided by the multishelled structure enlarges the electrode/electrolyte interface and exposes more active sites for sodium storage, thus leading to a continuous increase in capacity associated with pore-filling processes. Therefore, the rational design of C-HoMS through precise modulation of key structural parameters (e.g., shell number, shell thickness, and cavity volume) plays a decisive role in improving their performance. Extensive studies have verified the advantages of precise structural regulation and controllable synthesis in boosting the sodium storage performance of C-HoMS. For instance, Bu *et al*. [73] employed dopamine hydrochloride as the carbon precursor to fabricate double-shelled hollow hard carbon spheres (DHCSs) with a diameter of ~400 nm and a shell thickness of ~20 nm via a sacrificial template route. The as-prepared DHCSs possessed a high specific surface area of 673.7 $m^2\ g^{-1}$ and a large pore volume of 0.56 $cm^3\ g^{-1}$. When evaluated as SIB anodes, DHCSs delivered a high specific capacity of 113 mAh g^{-1} even at a high current density of 6 A g^{-1}, and maintained a stable capacity of 143.6 mAh g^{-1} after 1000 cycles at 0.6 A g^{-1}. In contrast, single-shelled hollow hard carbon spheres (SHCSs) exhibited inferior rate capability and lower cycling capacity (Figure 2F, G). The superior electrochemical performance of DHCSs is ascribed to the fact that the double-shelled architecture constructs a more robust conductive carbon network and integrated structure, which can maintain structural integrity and capacity stability with minimal volume variation, while ensuring rapid charge transfer kinetics across the electrode.

Beyond tailoring the shell numbers of C-HoMS, the optimization of chemical structures is equally decisive for their sodium storage performance. Heteroatom doping of C-HoMS can further facilitate fast electron transport and ion adsorption capability. Specifically, N-doped porous double-shelled hollow carbon spheres (N-DHCS) were successfully obtained using Fe_3O_4@C as the precursor, followed by chemical treatment with nitrogen-containing HNO_3 [74], as depicted in Figure 2H–J. It was revealed that the doped sample exhibited superior rate capability and cycling stability compared with the undoped sample (DHCS, treated with HCl). The introduction of nitrogen dopants induced the formation of carbon vacancies and an increase in electronic conductivity, which guaranteed more active sites for sodium storage and faster charge transfer kinetics, thus endowing the N-doped sample with prominent advantages over the undoped one. Similarly, Yu *et al*. [75] successfully prepared double-shelled hierarchically porous N-doped carbon nanocages (DHNCNs). Distinct from conventional spherical architectures, the as-synthesized DHNCNs inherited the morphological features of the ZIF-8 precursor, presenting well-defined nanocage structures. At different calcination temperatures, the DHNCNs exhibited significantly different physical and chemical states, which were reflected in specific surface area, defect concentration, and nitrogen content. In particular, when the temperature was set at 900 °C, the optimal states endowed the DHNCNs with the best sodium storage performance. Figure 2K compares the sodium storage characteristics of microporous N-doped carbon (MNC) and DHNCNs at this specific temperature. Benefiting from the synergistic effect of the abundant hierarchical porosity and multishelled architecture, the additional N doping further improved the conductivity of DHNCNs, providing robust support for rapid and efficient ion/electron transport. Beyond the commonly used N element, other nonmetallic dopants such as B [76,77], S [78,79], and P [80,81], as well as metallic dopants such as Bi [82]

and Zn [83], have also been demonstrated to be conducive to achieving high specific capacity, high ICE, and fast ion/electron transport kinetics.

Alloy-type HoMS

One of the prominent advantages of alloy-type anode materials is their ability to undergo alloying reactions with Na^+ during charge/discharge processes, which ensures an ultrahigh theoretical specific capacity and thus constitutes a critical route toward high-energy-density SIBs [84,85]. Typically, such materials include metals (e.g., Sn, Pb, Bi), metalloids (e.g., Si, Ge, As, Sb), and nonmetals (e.g., P). Figure 3A illustrates the typical sodium storage characteristics of these materials. Despite their strengths of low reaction potentials and high theoretical capacities, the alloying reactions with Na^+ induce significant volume expansion [86]. Under such circumstances, the assembled batteries suffer from intense internal stress, which triggers pulverization and detachment of electrode materials, leading to their separation from the current collectors and subsequent loss of electrochemical activity [84,87,88]. Furthermore, some alloy-type materials exhibit sluggish ion/electron transport kinetics, which will result in inferior rate and cycling performance under the condition of severe volume variation [89]. Therefore, maintaining high capacity while buffering volume strain during cycling has become one of the urgent challenges to be addressed for alloy-type anode materials. The introduction of HoMS provides an effective solution to these issues. During cycling, the hierarchical cavities offer ample buffer space to accommodate volume change, while the multishelled architecture restricts particle agglomeration and further pulverization, thus ensuring their structural stability. As reported in multiple studies, the electronic conductivity can be further improved by integrating carbon materials [90,91], especially when carbon constitutes the shell structure [92], which in turn ensures rapid ionic diffusion kinetics. Practically, the standalone design of pure alloy-type HoMS is rather difficult. Without the support of other substances, the HoMS architecture is prone to degradation due to significant volume expansion. Thus, the fabrication of high-performance alloy-type anodes typically relies on composite engineering with carbon materials or other functional additives.

Sn-based materials serve as one of the most appealing anode candidates for sodium storage, as the formation of $Na_{15}Sn_4$ alloy through multi-step sodiation processes delivers an ultrahigh theoretical specific capacity of 847 mAh g^{-1} (Figure 3B). Owing to the complicated sodiation mechanisms, the volume change of Sn can reach as high as 420% when transforming from a series of amorphous intermediates to the crystalline $Na_{15}Sn_4$ phase [93]. To address this issue, Wu *et al*. [94] employed hollow carbon spheres as nanoreactors, and sequentially introduced SnO_2 and MoS_2 precursors, followed by a reduction process to obtain double-shelled Sn/MoS_2@C composites. In this unique architecture with an outer carbon shell, MoS_2 is distributed throughout both the inner and outer shells, while Sn nanoparticles are interconnected with MoS_2 and primarily confined within the inner carbon layer (Figure 3C). The anchoring effect of Sn nanoparticles suppresses their further agglomeration, and the outer carbon shell prevents the detachment of free nanoparticles, thus yielding structurally robust alloy-type composites. Sb, another representative alloy-type material, exhibits high density and excellent conductivity due to its intrinsic wrinkled layered structure [95,96], rendering it a promising anode candidate for SIBs. Following a similar carbon-shell engineering strategy, Liu *et al*. [97] incorporated graphdiyne into the fabrication of HoMS, forming a composite material composed of an inner Sb hollow nanobox and an outer graphdiyne shell. This composite with a distinct

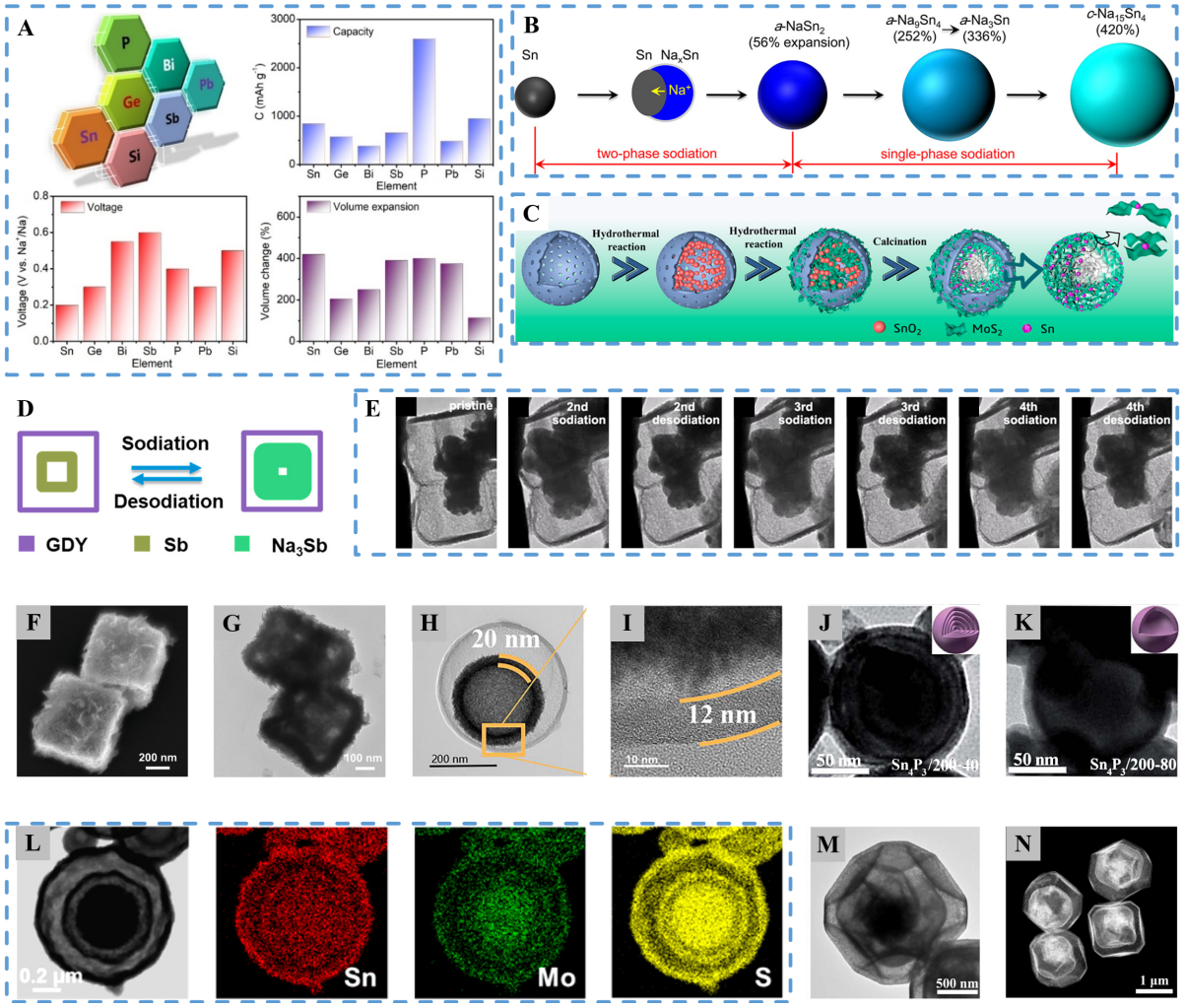

Figure 3 (A) Theoretical capacity, voltage plateau, and volume expansion rate of Bi, Sn, Sb, P, Pb, Si, and Ge alloy anodes. Reproduced with permission from Ref. [86]. Copyright©2024, Wiley-VCH GmbH. (B) Schematic illustration of the structural evolution of Sn NPs during the sodiation. Reproduced with permission from Ref. [93]. Copyright©2012, American Chemical Society. (C) Schematic illustration for synthesizing. Reproduced with permission from Ref. [94]. Copyright©2021, American Chemical Society. (D) Schematic of morphological evolution of hollow yolk–shell Sb@Void@GDY NBs during sodiation/desodiation. (E) *In situ* TEM images from time-lapse video of the first two to four sodiation-desodiation cycles. (D, E) Reproduced with permission from Ref. [97]. Copyright©2023, American Chemical Society. (F) SEM and (G) TEM images of Sb@C@TiO_2 TSNBs. Reproduced with permission from Ref. [98]. Copyright©2020, Wiley - VCH GmbH. (H) TEM and (I) HRTEM images of SnO_2-210@Void@HCSs. Reproduced with permission from Ref. [104]. Copyright©2022, Elsevier B.V. (J) TEM image of multishell Sn_4P_3 NSs prepared at 200 °C for 40 h. (K) TEM image of aggregated hollow Sn_4P_3 NSs prepared at 200 °C for 80 h. Reproduced with permission from Ref. [105]. Copyright©2017, The Royal Society of Chemistry. (L) Elemental mapping images of the yolk–shell SnS–MoS_2 composite microspheres. Reproduced with permission from Ref. [106]. Copyright©2015, American Chemical Society. (M) TEM and (N) STEM images of multi-shell Sb_2S_3. Reproduced with permission from Ref. [107]. Copyright©2019, Elsevier Ltd.

double-shelled hollow architecture demonstrated exceptional structural stability. As shown in Figure 3D, E, the schematic illustration of volume variation during charge/discharge cycles and the *in-situ* transmission electron microscopy (TEM) observations of the actual volume evolution process can be distinctly identified. After repeated cycling, the hollow architecture remained intact without noticeable collapse, which is attributed to the synergistic buffer effect of the cavity of the Sb nanobox and the interlayer cavity between Sb and graphdiyne. Meanwhile, the graphdiyne shell exerted a confinement effect on the expansion and aggregation of Sb. Similarly, by introducing TiO_2 as the third shell, Sb@C@TiO_2 triple-shelled nanoboxes

(TSNBs) can be readily fabricated on the basis of Sb@C nanostructures (Figure 3F, G) [98]. For pure alloy-type materials, the key to constructing HoMS lies in utilizing the internal cavities to provide sufficient buffer space for volume expansion. In addition, the incorporation of carbon or other functional materials as additional shells is beneficial for suppressing the expansion and agglomeration, as well as enhancing ion/electron transport kinetics.

For compounds containing alloy-type sodium-storage elements, their sodiation processes generally involve alloying reactions, as exemplified by oxides and sulfides of Sn and Sb [99–102], as well as Sn_4P_3 [103]. These compounds typically undergo an initial conversion reaction to form the corresponding alloy-type elemental phases, followed by subsequent alloying reactions, thus suffering from more severe volume variation issues. As illustrated in Figure 3H, I, the as-prepared SnO_2@C double-shelled hollow spheres feature an inner hollow SnO_2 shell with a thickness of 20 nm and an outer carbon shell of 12 nm. Although this architecture delivered a stable sodium-storage capacity of 335.6 mAh g^{-1} after 500 cycles at a current density of 1 A g^{-1} [104], its electrochemical performance can be further enhanced by structural optimization. The conversion reaction of SnO_2 and the subsequent alloying reaction of Sn require sufficient cavities to maintain structural stability. However, excessively large cavity volumes would weaken the dominant role of active materials, resulting in unsatisfactory energy density. More importantly, the design strategy for HoMS of such materials can be diversified: multishelled structures composed of the same substance can be readily fabricated, rather than constructing shells with different compositions. For instance, in the solvothermal reaction using Sn and white phosphorus as raw materials, single- and multi-shelled Sn_4P_3 nanostructures were successfully synthesized by simply controlling the reaction duration (Figure 3J, K) [105]. Comparative characterizations reveal that the multi-shelled Sn_4P_3 possesses 4–5 shells with an optimized cavity volume, which ensures a high specific surface area and superior sodium-storage capacity. At a current density of 50 mA g^{-1}, the multi-shelled Sn_4P_3 achieved a high specific capacity of 727 mAh g^{-1}, whereas the single-shelled sample exhibited a capacity of less than 600 mAh g^{-1}. These results demonstrate that for HoMS, a larger cavity volume does not equate to better performance. Instead, a delicate balance between cavity volume and shell number is essential to simultaneously preserve structural integrity and achieve high capacity and energy density. Over the past decades, a wide variety of HoMS architectures have been designed for sodium-storage anodes, such as SnS-MoS_2 (Figure 3L) [106] and Sb_2S_3 (Figure 3M, N) [107]. The successful synthesis and application of these materials not only verify the superiority of HoMS in sodium storage but also clarify the critical roles of structural parameters in governing electrochemical performance, thereby providing novel insights into the rational design of high-performance conversion-alloying type anode materials.

Conversion-type HoMS

Metal compounds, such as oxides [108,109], sulfides [110–112], selenides [61,113,114], and phosphides [115,116], are widely investigated conversion-type anode materials, where the metal components typically include Mn, Fe, Co, Ni, W, and other transition metals. Unlike intercalation and alloying reactions, such conversion reactions involve the cleavage of intrinsic chemical bonds and the formation of new bonds during the generation of sodium-containing compounds [117]. In other words, conversion reactions are analogous to displacement reactions, accompanied by the formation of corresponding metallic elements during the

discharge process (Figure 4A), a reaction mechanism that is also applicable to LIBs [118]. In the case of FeS_2, the initial sodiation process yields Na_xFeS_2, which further reacts with Na^+ to form the final products of Fe and Na_2S [119]. Despite their appealing theoretical specific capacity derived from the multi-electron conversion mechanism, these metal compounds still suffer from several critical issues that require further optimization. For instance, the low ICE, inferior electronic conductivity, and severe volume expansion can collectively lead to poor rate capability and irreversible capacity decay during cycling [120–122]. To address these challenges, the rational construction of HoMS is demonstrated to be an effective strategy for boosting the sodium storage capacity and improving the cycling stability of such materials.

Metal oxides represent one of the earliest investigated categories of metal compounds. As early as 2002, Alcántara *et al*. [123] first reported and demonstrated the potential of $NiCo_2O_4$ as an anode material for sodium storage, introducing the concept of the conversion mechanism. In the subsequent decades, $NiCo_2O_4$ anodes have been successively reported and proven to exhibit favorable sodium storage performance [124,125]. For instance, double-shelled $NiCo_2O_4$ synthesized via microwave-assisted solvothermal method delivered a specific capacity of 511 mAh g^{-1} at a current density of 100 mA g^{-1}, with a capacity retention of 66% after 100 cycles [126]. When fabricating hollow multishelled V_2O_3/C composites, Li *et al*. [127] found that an increased number of shells contributes to higher specific capacity and superior rate capability. As illustrated in Figure 4B, during the investigation into the formation mechanism of multishelled architectures, it was revealed that the time-dependent process relies on the diffusion and crystallization of vanadium species. Wang's group [128] further verified via numerical simulation and experimental validation that the formation of HoMS is essentially attributed to the existence of concentration waves (Figure 4C). Therefore, the generation of appropriate concentration waves is indispensable for the preparation of HoMS via a sequential templating approach. Based on this principle, WO_3 HoMS was successfully fabricated, and WS_{2-x} HoMS with sulfur vacancies was derived via sequential sulfidation and etching procedures (Figure 4D) [129]. This multishelled architecture exhibited exceptional rate capability, retaining a high specific capacity of 191 mAh g^{-1} even at a high current density of 10 A g^{-1}. Furthermore, the assembled pouch cell could readily power a light-emitting diode (LED) screen and maintained a high reversible capacity of 294.6 mAh g^{-1} after 300 cycles (Figure 4E, F), demonstrating remarkable practical application potential.

In fact, the conversion reaction mechanisms of transition metal sulfides (TMSs) are highly analogous to those of their oxides. Owing to the weaker metal–sulfur bonds compared with the corresponding metal–oxygen bonds, TMSs are kinetically more favorable for the occurrence of conversion reactions [130]. As shown in Figure 4G–J, the scanning electron microscopy (SEM) images of CoS_2 HoMS with 2–5 shells clearly reveal their well-defined nanocubic morphology [131]. When employed as anode materials, these multishelled architectures all exhibited exceptionally stable cycling performance. Similarly, multishelled heterostructures of polymetallic sulfides, such as CuS@CoS_2 [132] and $Cu_{39}S_{28}$-CoS_2-ZnS [133], have also been successfully fabricated for SIB applications. The design superiority of multishelled polymetallic sulfides lies in the facile formation of heterogeneous interfaces among different components. The lattice matching at these interfaces facilitates the construction of built-in electric fields, which in turn drive rapid Na^+ diffusion and reduce the energy barrier. As illustrated in Figure 4K, L, Chen *et al*. [134] synthesized triple-shelled FeS/MoS_2@NC hollow nanostructures and systematically investigated the effect of the heterostructure on Na^+ storage performance. In comparison with pristine FeS and MoS_2, the FeS/MoS_2 heterointerfaces possessed more favorable Na^+ adsorption energy and lower Na^+ diffusion energy barrier

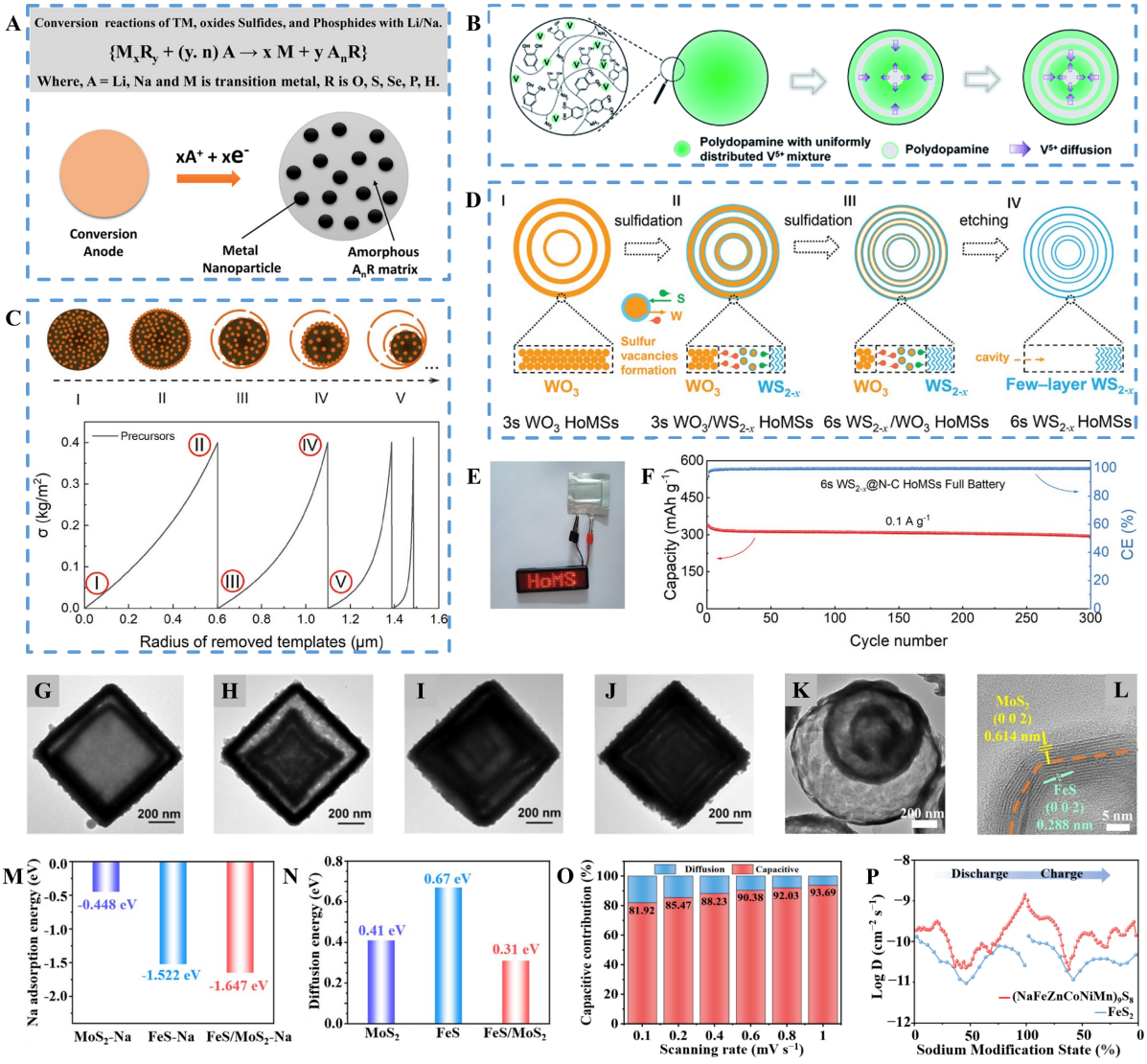

Figure 4 (A) Li/Na-storage mechanism in conversion-type anodes. Reproduced with permission from Ref. [118]. Copyright©2018, American Chemical Society. (B) Schematic illustration of the formation mechanism for the multi-shelled structure. Reproduced with permission from Ref. [127]. Copyright©2019, The Royal Society of Chemistry. (C) Variation of the σ during the template removal process and the schematic illustrations of labeled states. Reproduced with permission from Ref. [128]. Copyright©2023, Wiley‐VCH GmbH. (D) Illustration of the synthesis process of 6s WS_{2-x} HoMSs. (E) Optical image of an LED screen powered by the pouch cell. (F) Long cycle performance of the 6s WS_{2-x}@N-C HoMSs//$Na_3V_2(PO_4)_3$@C SIB full cells. (D–F) Reproduced with permission from Ref. [129]. Copyright©2022, Wiley‐VCH GmbH. (G–J) TEM images of cobalt sulfide DSNBs, TSNBs, QuaSNBs, and QuiSNBs, respectively. Reproduced with permission from Ref. [131]. Copyright©2019, Wiley‐VCH Verlag GmbH & Co. KGaA, Weinheim. (K) TEM and (L) HRTEM images of T-FeS/MoS_2@NC. (M) Na^+ adsorption binding energies for different surfaces. (N) Na^+ diffusion energy barriers for MoS_2, FeS, and FeS/MoS_2. Reproduced with permission from Ref. [134]. Copyright©2025, The Author(s). (O) Pseudocapacitive contribution of $(NaFeZnCoNiMn)_9S_8$ at different scan rates. (P) Changes in Na^+ diffusion coefficients during the charge and discharge process. (O, P) Reproduced with permission from Ref. [135]. Copyright©2025, The Author(s).

(Figure 4M, N), which corroborates the critical role of the built-in electric field. Distinct from single interfaces, the heterointerfaces in HoMS exhibit a 3D hierarchical distribution, which not only enables higher active site utilization but also fully exploits the structure–interface synergistic effect, thus providing an advanced solution for the practical demands of high-rate and long-cycling SIBs. With the further in-

corporation of additional metal elements, high-entropy sulfides can also be engineered into HoMS [135]. The high-entropy effect further induces the formation of built-in electric fields. Meanwhile, the stress dispersion within the lattice and multiphase interface confinement derived from high-entropy design further suppresses volume variation at the atomic and microscale. Furthermore, the synergistic effect of multi-element doping and multishelled architecture jointly realizes enhanced pseudocapacitive behavior and elevated Na^+ diffusion coefficients (Figure 4O, P), thereby improving the rate performance. TMSs have long been recognized as attractive anode materials for sodium storage. When rationally designed into HoMS, they exhibit more abundant Na^+ storage sites, faster ion/electron transport kinetics, and superior overall electrochemical performance.

HOMS FOR CATHODE OPTIMIZATION

Owing to the larger ionic radius of Na^+, cathode materials for SIBs cannot be directly adopted from their LIB applications, which is a distinct difference from the anode materials. Cathode materials contain active Na^+ and generally exhibit high redox potentials, which are directly correlated with key metrics such as energy density and cycle life [136]. Therefore, the structure and functionality of cathode materials are crucial to the electrochemical performance of SIBs. Specifically, they must possess the capability for highly reversible Na^+ intercalation/deintercalation as well as excellent ionic/electronic conductivity to ensure ideal sodium storage performance.

Currently, research efforts for SIB cathode materials mainly focus on transition metal oxides (TMOs) [137–139], polyanionic compounds (PCs) [140–142], Prussian blue (PB) [143,144] and its analogues (PBAs) [145–147], etc. They have their own merits, but also suffer from inherent drawbacks. TMOs usually deliver inferior rate performance, and layered oxides, in specific, are limited by structural collapse and transition metal ion dissolution [148]. PCs feature high thermal stability and safety, yet they are limited by poor electronic conductivity and sluggish ionic diffusion kinetics [149]. For PBs and PBAs, their frameworks contain abundant defects and crystal water, which significantly reduce the active sites for sodium storage [150].

HoMS exhibits unique advantages in effectively improving the electrochemical performance of cathode materials. By rationally tailoring the structural parameters and compositions of HoMS, the following goals can be achieved: (1) shortening the Na^+ diffusion pathways to enhance ion transport efficiency; (2) enlarging the electrode/electrolyte contact area to promote interfacial charge transfer kinetics; (3) alleviating volume expansion and structural deformation to improve structural stability; (4) suppressing the dissolution of transition metal ions to reduce the loss of active species. In the following sections, the optimization strategies and underlying mechanisms of HoMS will be discussed in detail for different types of cathode materials.

Metal oxides-based HoMS

TMOs represent one of the most extensively investigated cathode materials for SIBs, featuring high theoretical capacities and high redox potentials. Common structural types include O3-type, P2-type, and tunnel-type configurations [151]. Taking layered oxides as a typical example, they often exhibit distinct structural

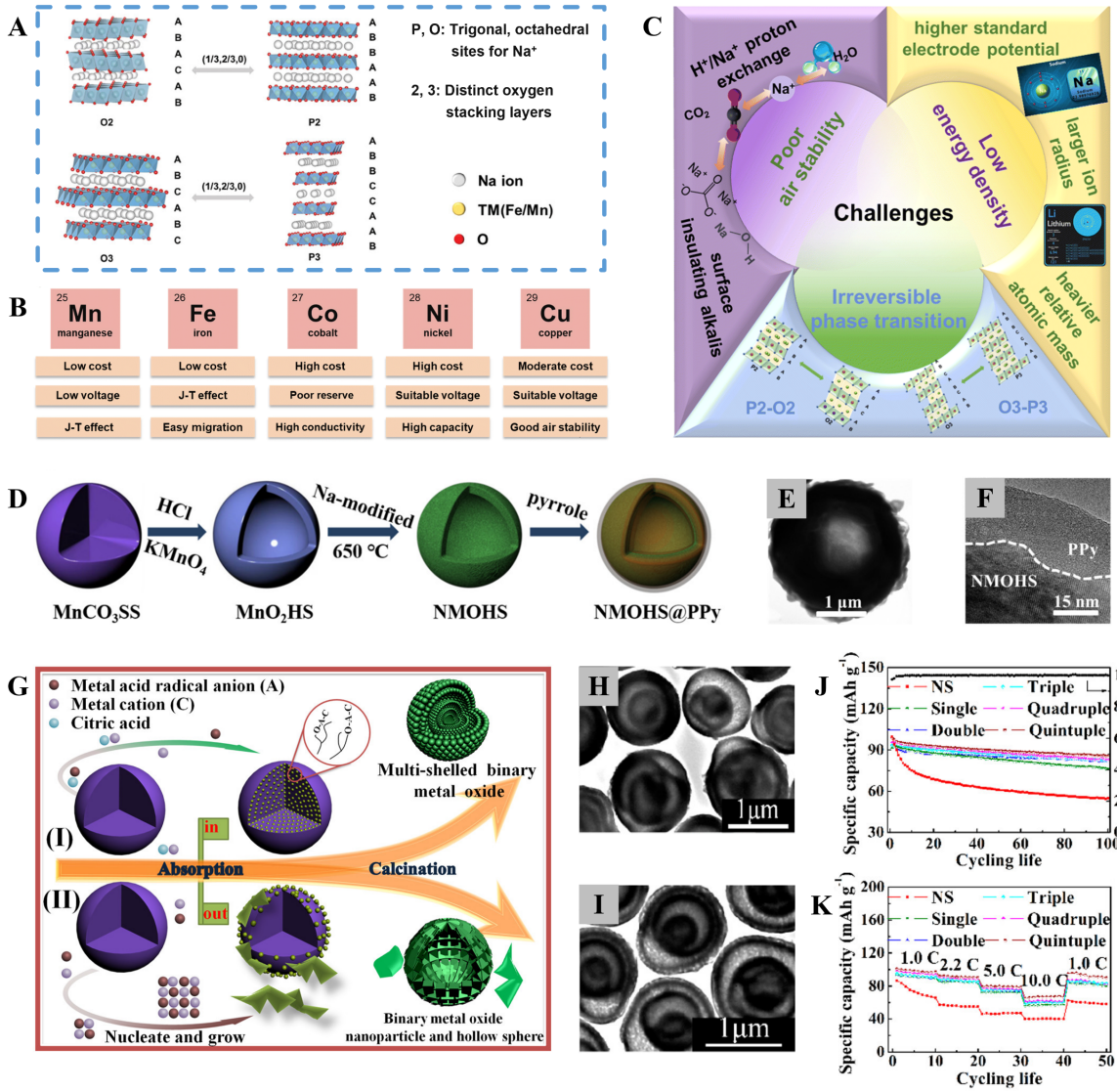

Figure 5 (A) Four types of layered oxide cathode materials: O2, O3, P2, and P3. P and O represent different polyhedral coordination environments of sodium ions, O indicates that Na ions are located in the octahedral coordination center, and P represents Na ions located in the triangular prismatic coordination center. The number represents the TMO_6 octahedral layer stacked with oxygen ions. Reproduced with permission from Ref. [152]. Copyright©2024, Wiley‐VCH GmbH. (B) Features of Mn-, Fe-, Co-, Ni-, and Cu-based redox in layered oxides. Reproduced with permission from Ref. [153]. Copyright©2024, The Royal Society of Chemistry. (C) Challenges associated with layered oxide cathode for SIBs. Reproduced with permission from Ref. [154]. Copyright©2024, The Royal Society of Chemistry. (D) Schematic illustration for the fabrication of NMOHS and NMOHS@PPy. (E, F) TEM images of NMOHS@PPy. (D–F) Reproduced with permission from Ref. [156]. Copyright©2019, American Chemical Society. (G) Process for synthesizing multishelled binary metal oxide hollow spheres. (I) With citric acid, the precipitation reaction was extremely restrained due to the chelation of citric acid; thus, metal ions can penetrate into the inside of the CMS templates, resulting in multishelled hollow spheres. (II) Without citric acid, the precursor of the binary metal oxide will be precipitated on the surface of carbon microspheres, resulting in nanoparticles and irregular single-shelled hollow spheres. (H) TEM image of quadruple-shelled hollow spheres. (I) TEM image of quintuple-shelled hollow spheres. (J) Cycling life test and (K) rate performance of $Fe_2(MoO_4)_3$ NS and multishelled $Fe_2(MoO_4)_3$ hollow spheres as cathode materials for sodium-ion batteries. (G–K) Reproduced with permission from Ref. [157]. Copyright©2018, American Chemical Society.

characteristics and sodium storage behaviors owing to their various chemical compositions (Figure 5A) [152]. In addition, the type of transition metal incorporated also exerts a profound impact on the overall electrochemical performance [153]. For instance, Co-based materials are beneficial for enhancing charge

transport kinetics, Cu-based materials contribute to improved cycling stability, and Fe-based materials are more suitable for large-scale production with cost-effectiveness (Figure 5B). Nevertheless, layered oxides are confronted with several urgent issues to be addressed, such as ambient-air instability, low energy density, and irreversible phase transitions (Figure 5C) [154]. Furthermore, problems, including structural collapse and transition metal ion dissolution, also influence their sodium storage performance. The introduction of HoMS offers an effective strategy to improve the electrochemical performance of TMOs. On the one hand, the enlarged specific surface area shortens Na^+ diffusion pathways, thus ensuring highly efficient ion transport kinetics. On the other hand, for some metal oxides with inferior electronic conductivity, surface coating of each shell with highly conductive materials enables enhanced conductivity, which is conducive to suppressing transition metal ion dissolution and improving structural stability.

Layered sodium manganese oxides can exhibit high theoretical specific capacities and good Na^+ conductivities, rendering them a promising cathode material for SIBs [155]. However, their low electronic conductivity and the dissolution of Mn fail to meet the requirements of rapid charge/discharge processes, resulting in inferior rate capability and cycling performance. To address these issues, Lu *et al*. [156] fabricated polypyrrole (PPy)-coated $Na_{0.7}MnO_{2.05}$ hollow microspheres (NMOHS@PPy) using MnO_2 as the precursor, as illustrated in Figure 5D. The resultant NMOHS@PPy possesses a distinct hollow architecture and a uniform surface coating layer, with a well-matched cavity volume that avoids superfluous space (Figure 5E, F). When employed as a cathode material for SIBs, this structure delivered a specific capacity of 165.1 mAh g^{-1} at 0.1 A g^{-1}, with a capacity retention of 88.6% after 100 cycles. Even when the current density was increased to 2 A g^{-1}, NMOHS@PPy still maintained a high specific capacity of 100.5 mAh g^{-1}. In contrast, the solid $Na_{0.7}MnO_{2.05}$ microspheres only retained 29.6 mAh g^{-1} at the same high current density. These results demonstrate that the hollow structure combined with surface coating guarantees enhanced rate capability and cycling stability, where the coating layer can effectively prevent Mn dissolution during cycling. As shown in Figure 5G, Zhao *et al*. [157] adopted a facile cation/anion co-adsorption method in the synthesis of cathode materials, utilizing citric acid to suppress hydrolysis and precipitation effects, thus successfully preparing a series of bimetallic oxides including $Fe_2(MoO_4)_3$, $NiMoO_4$, $MnMoO_4$, $CoWO_4$, and $MnWO_4$. Taking $Fe_2(MoO_4)_3$ as an example, its crystallinity and shell number can be precisely tailored by adjusting the key parameters during the synthesis process. As illustrated in Figure 5H, I, the representative architectures with four and five shells are clearly observed. Notably, the quintuple-shelled $Fe_2(MoO_4)_3$ delivered a specific capacity of 85.6 mAh g^{-1} after 100 cycles at a current density of 2.2 C (Figure 5J). The rate performance presented in Figure 5K also confirms its superior capacity retention capability, achieving a high specific capacity of 67.4 mAh g^{-1} even at 10 C. It can be observed that $Fe_2(MoO_4)_3$ with multishelled architectures exhibits more favorable cycling performance and rate capability than the nanosheets, and the performance enhancement becomes more pronounced with an increasing number of shells. These findings verify the unique advantages of HoMS in metal oxide cathode materials. Nevertheless, relevant reports remain relatively scarce, and the underlying structure-property relationships as well as performance optimization mechanisms still require further investigation to fully explore the potential of HoMS.

Polyanionic compounds-based HoMS

PCs represent another type of promising cathode materials for SIBs, whose structures consist of tetrahedral

anionic units $(XO_4)^{n-}$ and their derivatives $(X_mO_{3m+1})^{n-}$ (X = S, P, etc.), as well as polyhedral units MO_x (M = transition metals) [158−160]. Notably, in contrast to layered oxides, the strong covalent X–O bonds within these compounds can induce a higher degree of ionization of the M–O bonds, thus endowing them with high operating voltages [161]. The sodium storage mechanisms of these materials rely on the intercalation/deintercalation of Na^+ within the polyanionic frameworks. Benefiting from the high structural stability of the frameworks, such materials generally exhibit excellent cycling stability. However, PCs suffer from intrinsically poor electronic conductivity and sluggish ionic diffusion kinetics, thus failing to meet the demands of high-power energy storage applications. The design of HoMS can improve the electronic conductivity and ionic diffusion dynamics of PCs. An enlarged electrode/electrolyte contact area can significantly reduce the resistance of ion diffusion and electron transport. Simultaneously, the efficient utilization of active materials is facilitated by the hierarchical hollow structure, which also ensures uninterrupted electrolyte supplementation and transportation and reduces the ion/electron transfer barrier [162].

$Na_3(VOPO_4)_2F$ (NVPOF) is a type of PC containing a small amount of fluorine. Its electrochemical reactions are generally limited to the transfer of two electrons in each structural unit, leading to a theoretical specific capacity of less than 150 mAh g^{-1} [163]. Nevertheless, the inductive effect induced by fluorine is favorable for Na^+ diffusion, rendering NVPOF a research focus. In 2018, Qi *et al*. [164] successfully synthesized hollow multishelled NVPOF on a large scale at room temperature (Figure 6A, B), which involves a facile synthetic process with mild reaction conditions. It is worth noting that each shell of this HoMS is assembled from nanocrystals, and it can achieve superior electrochemical performance without any surface coating or high-temperature treatment. When employed as a cathode material, the multishelled NVPOF delivered a specific capacity of 111 mAh g^{-1} at a current density of 0.1 C, and still retained a specific capacity of 73.4 mAh g^{-1} even at a high rate of 15 C, demonstrating outstanding rate capability. The presence of multiple shells shortens the Na^+ diffusion pathways, and the nanocrystals on each shell further enhance this effect, providing structural support for rapid ion diffusion. After 3000 cycles at 15 C, the multishelled NVPOF maintained a capacity retention of 70% (Figure 6C), enabling rapid charge/discharge processes within several minutes. Theoretically, the large specific surface area of HoMS provides abundant sodium storage sites, while the arrangement of hierarchical shells shortens the ion/electron transport pathways, thereby overcoming the intrinsic limitations of PCs. Another study focused on the formation mechanism of porous yolk-shell NVPOF during the solvothermal process [165]. As shown in Figure 6D–H, solid microspheres gradually transform into hollow structures with the extension of reaction time. However, prolonged Ostwald ripening leads to the disappearance of the hollow architecture. This synthetic process of hollow structures based on the self-sacrificial template and Ostwald ripening mechanisms reflects the dominant role of reaction parameters. Rational control of the kinetic parameters during the sacrificial template or self-assembly process enables the precise regulation of the material evolution process. Typically, such control protocols require the combination of *in-situ* characterization techniques to facilitate the investigation of material states under different conditions. Based on this, HoMS can be more extensively applied in the synthesis of PCs.

Fe-based PCs are another type of appealing cathode material, attributed to their low cost and environmental friendliness [166]. Na_2FePO_4F (NFPF) is a typical doped Fe-based material, whose 2D layered structure provides facile diffusion pathways for Na^+, with its detailed crystal structure illustrated in Figure 6I [167]. When carbon-coated double-shelled hollow NFPF was employed as the cathode material for SIBs

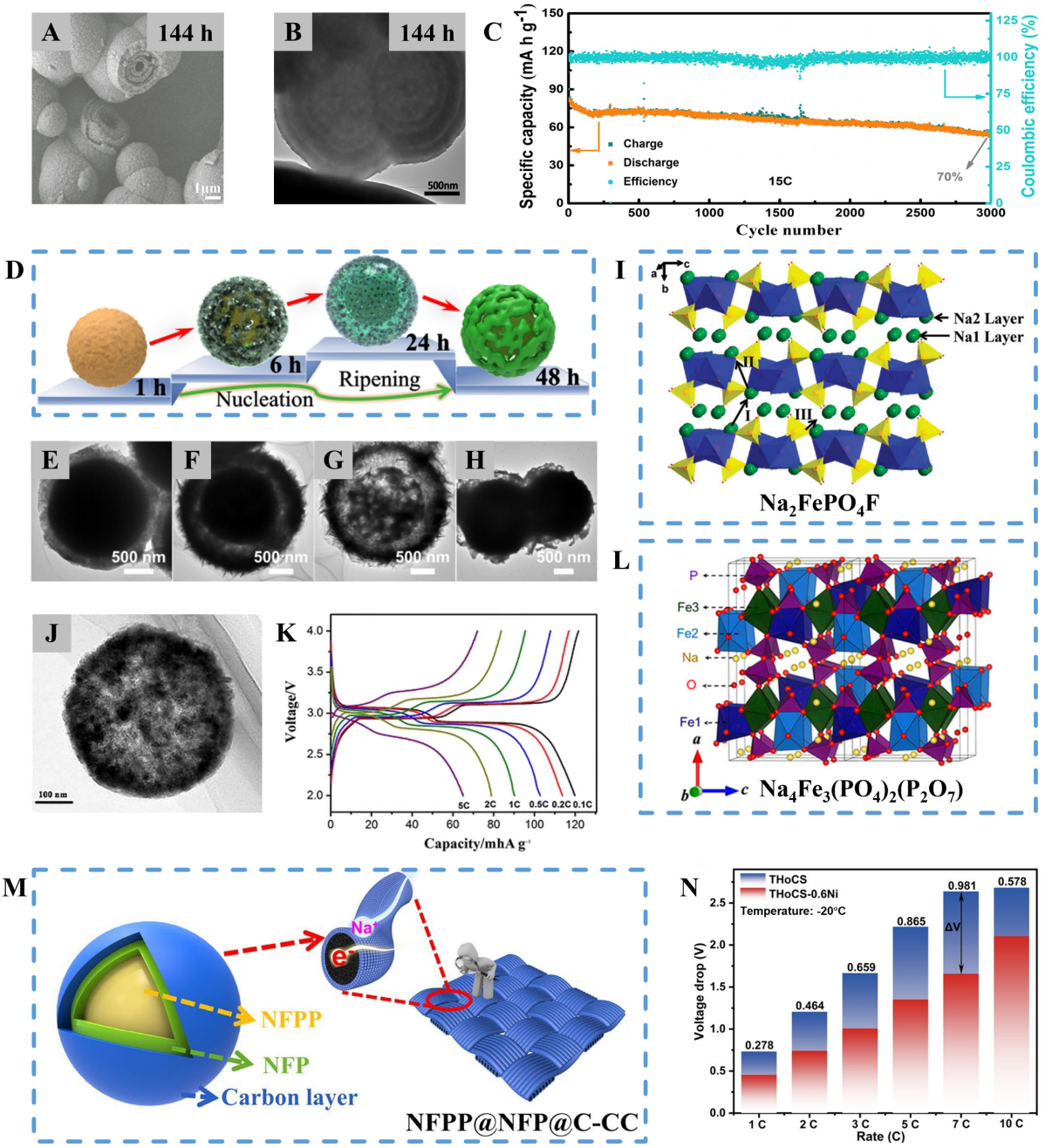

Figure 6 (A) SEM and (B) TEM images of NVPOF at 144 h. (C) The cycling performance of NVPOF electrode at a current rate of 15 C. (A–C) Reproduced with permission from Ref. [164]. Copyright©2018, Elsevier Inc. (D) Schematic illustration of the time-dependent solvothermal reaction: self-sacrifice and Ostwald ripening mechanism from rough spheres to yolk-shell structure. (E–H) TEM images of products synthesized with different solvothermal times (1, 6, 24, and 48 h, respectively). Reproduced with permission from Ref. [165]. Copyright©2021, Elsevier. (I) Crystal structure of Na_2FePO_4F: view along [100]. Ion transport pathways (I, II, and III) are marked. Reproduced with permission from Ref. [167]. Copyright©2009, American Chemical Society. (J) TEM image of the as-synthesized double-shelled hollow Na_2FePO_4F/C sample. (K) Charge and discharge profiles of double-shelled hollow Na_2FePO_4F/C sample at various current rates. (J, K) Reproduced with permission from Ref. [168]. Copyright©2017, Springer Science Business Media, LLC. (L) Schematic of $Na_4Fe_3(PO_4)_2(P_2O_7)$. Reproduced with permission from Ref. [169]. Copyright©2025, The Author(s). (M) Schematic illustration of NFPP@NFP@C-CC flexible electrode. Reproduced with permission from Ref. [171]. Copyright©2019, Elsevier B.V. (N) Voltage drops of THoCS and THoCS-0.6Ni at different rates. Reproduced with permission from Ref. [172]. Copyright©2024, Wiley-VCH GmbH.

(Figure 6J), it delivered a reversible specific capacity of 120.1 mAh g^{-1} at 0.1 C, corresponding to 96.9% of the theoretical specific capacity [168]. As shown in Figure 6K, voltage plateaus at 3.07 and 2.91 V are observed in the charge/discharge profiles, indicating negligible polarization during the Na^+ intercalation/deintercalation processes. In contrast, $Na_4Fe_3(PO_4)_2(P_2O_7)$ (NFPP) features a completely distinct crystal structure. Figure 6L displays the crystal structure of this hybrid polyanionic material, where the constructed continuous 3D network enables 3D diffusion pathways for Na^+ [169]. Xia *et al*. [170] synthesized NFPP/C hollow microspheres via spray drying followed by calcination, which exhibited a higher specific surface area compared with pristine NFPP without carbon coating or hollow architecture. The carbon coating on the shell surface can enable superior electronic conductivity of the material, thereby boosting its sodium storage performance. Similarly, Figure 6M presents a schematic illustration of the synthesis for double-layer coating of $NaFePO_4$ (NFP) and carbon on the NFPP surface. This method enables direct growth on carbon cloth, yielding a binder-free integrated cathode material (NFPP@NFP@C-CC). As expected, NFPP@NFP@C-CC achieved a high specific capacity of 68 mAh g^{-1} even at an ultrahigh current density of 100 C, and retained nearly no capacity fading after 3000 cycles at 10 C, demonstrating the superiority of multi-layer coating [171]. However, no obvious cavities are observed due to the *in-situ* growth on carbon cloth. Qi *et al*. [172] further improved the electrochemical performance of NFPP via a synergistic strategy combining Ni doping, hollow structure, and shell structure modification. It is found that the as-prepared hollow core-shell $Na_4Fe_{2.4}Ni_{0.6}(PO_4)_2P_2O_7$ (THoCS-0.6Ni) possesses abundant microporous spaces, which together with the cavities facilitate sufficient electrolyte-wettability to realize rapid and efficient ion diffusion. Meanwhile, Ni doping further improves the intrinsic electronic conductivity and ionic diffusion kinetics of NFPP, which is evidenced by the reduced voltage plateau drops with increasing current densities (Figure 6N). Collectively, these results suggest that the synergistic effects of hollow structure, shell configuration, and elemental doping on the optimization of PCs are conducive to obtaining high-performance SIBs with fast-charging capability and low-temperature storage characteristics.

Prussian blue- and its analogues-based HoMS

Fe-based PB ($Na_xFe[Fe(CN)_6]$) and PBAs ($Na_xM[Fe(CN)_6]$, where M represents other transition metals) are a class of coordination polymers with cubic structures [173], as illustrated in Figure 7A. Benefiting from their open frameworks, these materials typically exhibit large ionic channels and lattice interstices, which are highly favorable for rapid Na^+ diffusion, thus endowing them with excellent rate capability [174,175]. In general, the Fe element in PB-based materials can be readily substituted by other transition metals, enabling the fabrication of cathode host materials with analogous structures yet distinct electrochemical performance. Nevertheless, PBAs usually suffer from poor crystallinity, accompanied by abundant structural defects and crystal water [176–178]. These issues will lead to structural collapse during charge/discharge cycles, which severely affects their electrochemical performance. Specifically, the coordination of water molecules with metal ions reduces the Na^+ storage sites, while the water molecules themselves impede Na^+ diffusion [179–181]. In organic electrolytes, the presence of water not only deteriorates the electrolyte stability but also poses potential safety hazards [182,183]. The design of PBAs into HoMS offers a significant method to address these aforementioned issues. On the one hand, HoMS can enhance the crystallinity and mitigate the side effects of defects and water molecules. On the other hand, the construction of composite HoMS via

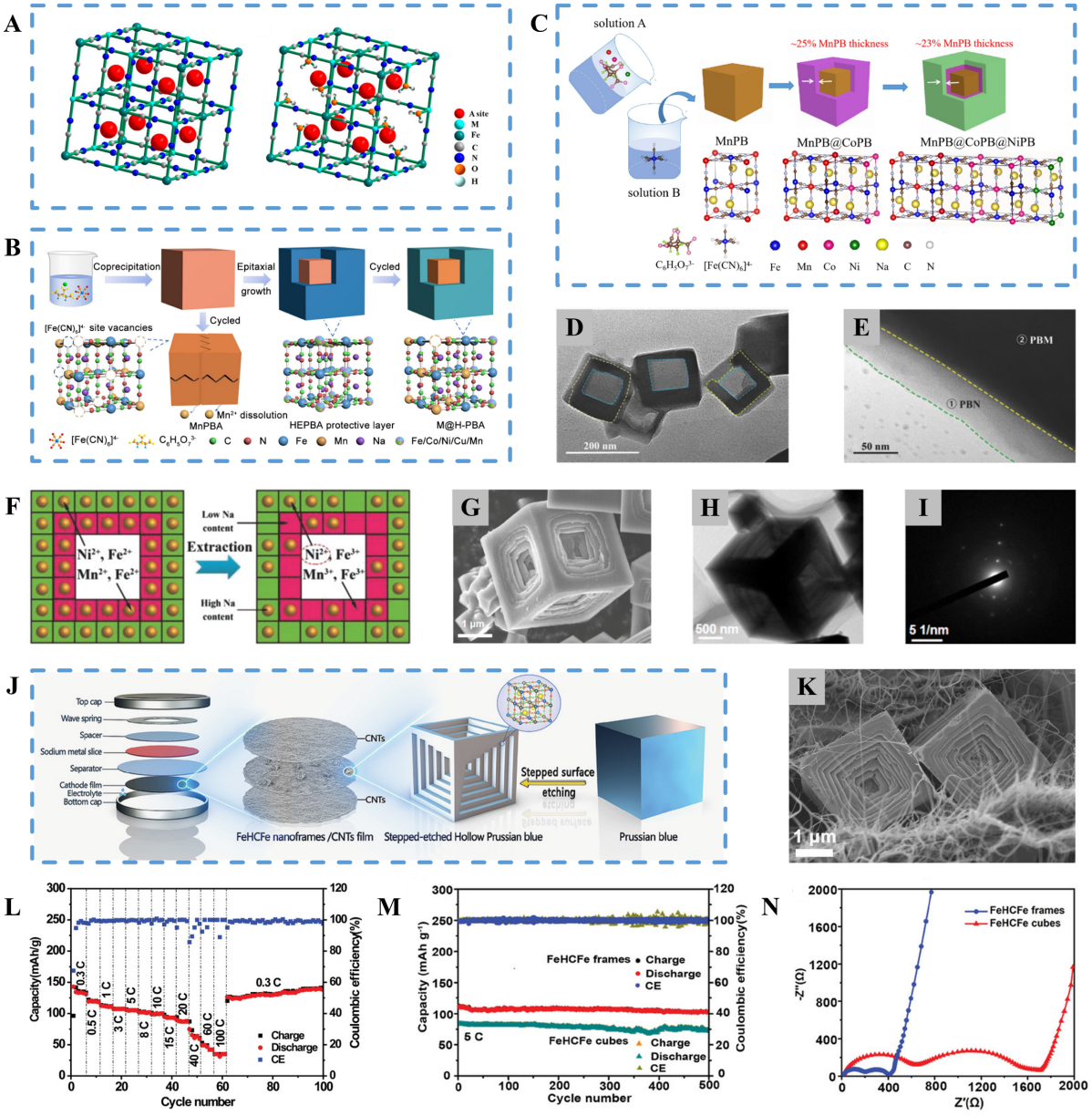

Figure 7 (A) Schematic crystal structures of Prussian blue frameworks. Reproduced with permission from Ref. [173]. Copyright©2016, American Chemical Society. (B) Schematic illustration of the synthetic route of M@H-PBA. Reproduced with permission from Ref. [187]. Copyright©2025, American Chemical Society. (C) Schematic illustration of NiCoMnPB synthesized by a simple one-pot method. Reproduced with permission from Ref. [188]. Copyright©2024, Elsevier B.V. (D, E) TEM images at different magnifications of HCS-PBMN samples. (F) Schematic illustration of the extraction process of Na^+ ions. (D–F) Reproduced with permission from Ref. [189]. Copyright©2018, Wiley‐VCH Verlag GmbH & Co. KGaA, Weinheim. (G) SEM, (H) TEM images, and (I) SAED pattern of BTA-PB-1.6. (G–I) Reproduced with permission from Ref. [190]. Copyright©2024, American Chemical Society. (J) Sketch map of nanostructure engineering route for a stepwise hollow PBA nanoframes/CNTs cathode. (K) Field emission (FESEM) image of FeHCFe nanoframes/CNTs composites. (L) Test performance at high rates for FeHCFe nanoframe/CNTs composite cathode materials. (M) Cycle performance of the FeHCFe nanoframes/CNTs and FeHCFe nanocube/CNTs composite cathode materials at 5 C. (N) The impedance spectrum of both FeHCFe nanoframes/CNTs and FeHCFe nanocube samples. (J–N) Reproduced with permission from Ref. [191]. Copyright©2020, Wiley-VCH Verlag GmbH & Co. KGaA, Weinheim.

hybridization with other materials can not only further improve the electronic conductivity but also optimize the electrode/electrolyte interface, thereby enhancing the ionic diffusion kinetics.

Mn-based PBAs are attractive cathode materials, which exhibit high theoretical specific capacity and high operating voltage due to the substitution of Mn [184]. However, the specific Jahn-Teller effect and ion dissolution give rise to irreversible capacity loss, thus resulting in inferior cycling performance [185,186]. Thus, constructing a coating layer on the surface of Mn-based PBAs can effectively mitigate these drawbacks. Ji *et al*. [187] improved the intrinsic low conductivity and prevented Mn dissolution via self-assembling a special epitaxial thin layer on the Mn-based PBAs (M@H-PBA), as illustrated in Figure 7B. Notably, this epitaxially grown layer was also a high-entropy PBA, ensuring that the obtained core-shell structure delivered a high capacity retention of 81.8% after 1000 cycles at 1 A g^{-1}. Similarly, a multilayer cathode material, namely MnPB@CoPB@NiPB, was successfully achieved through multiple epitaxial growth processes (Figure 7C) [188]. Although this epitaxial growth coating method can be extended to the preparation of PBAs with more layers, it is rather challenging to construct hollow parts on this basis. Hollow nanomaterials possess the advantages of a large specific surface area, low density, and abundant active sites. When combined with a multilayer structure, they can not only buffer volume expansion but also improve interfacial properties. In the preparation of hollow core-shell structures, the inhibitory effect of surfactants plays a crucial role, providing a facile route for the synthesis of hollow $Na_2MnFe(CN)_6$ coated with $Na_2NiFe(CN)_6$ (denoted as HCS-PBMN) [189]. As shown in Figure 7D, E, HCS-PBMN features a distinct hollow double-shelled structure, which is conducive to achieving low defect density and interfacial impedance. It is found that when charged to 4.2 V, the core and shell exhibit high and low Na contents, respectively (Figure 7F). This feature balances high capacity and high stability, endowing the material with outstanding rate capability (a specific capacity of 52 mAh g^{-1} at 3200 mA g^{-1}) and cycling stability (a specific capacity of 102 mAh g^{-1} after 600 cycles at 50 mA g^{-1}).

Wang *et al*. [190] exploited the chelating and etching effects of 1,3,5-benzenetricarboxylic acid (BTA) to construct a hierarchical hollow layered architecture on the entire surface of PB (BTA-PB-1.6), as illustrated in Figure 7G, H. The selected-area electron diffraction (SAED) results (Figure 7I) demonstrated that PB still maintained favorable crystallinity even after a series of etching processes, indicating the high reproducibility of this synthetic strategy. In another similar study, stepwise etched PB could be integrated with carbon nanotubes (CNTs) to prepare a hierarchical composite film, which was applied as a binder-free cathode for SIBs (Figure 7J) [191]. As shown in Figure 7K, the PB HoMS exhibited a distinct multilayer structure and was interconnected by CNTs, forming a 3D conductive network. The superior hollow layered structure coupled with the 3D network enabled rapid ion and electron transport, delivering a specific capacity of 35.0 mAh g^{-1} even at an ultrahigh rate of 100 C (Figure 7L). In comparison with the reference sample without the hollow multilayer structure and CNT incorporation, the synergistically optimized composite film exhibited better cycling stability and lower interfacial impedance (Figure 7M, N). Actually, owing to the presence of structural defects and unique topological nanostructures, PBs and PBAs are prone to being engineered into hollow structures [192,193]. Further combination with etching technology enables the fabrication of HoMS, thereby endowing the materials with enhanced tolerance to lattice expansion and improved ion/electron transport capability. Distinct from the extensively reported HoMS, the etching-derived HoMS belongs to open frameworks, which constitutes a unique advantage of PB and PBAs. The multiple internal shells and cavities are directly accessible to the electrolyte, thus exposing more active sites and further shortening the

ionic diffusion pathways [194,195]. Therefore, for PB and PBAs, novel multifunctional HoMS can be prepared according to their intrinsic characteristics, so as to broaden their applications as cathode materials for SIBs.

SUMMARY AND PERSPECTIVES

HoMS represents a novel and versatile material architecture with intrinsic structural-activity synergy, featuring hierarchical hollow cavities, tunable shell thickness, abundant porous networks, and a large specific surface area. These unique structural merits enable HoMS to address the core bottlenecks of SIBs through multi-dimensional regulation, thereby achieving intrinsic performance enhancement of electrode materials beyond mere physical optimization.

Unlike its auxiliary role in LIBs, HoMS serves an indispensable function in SIBs, with this divergence stemming from the fundamental differences in ionic behavior and reaction characteristics between Na^+ and Li^+. For anode materials (carbon-based materials, alloy-type materials, and transition metal compounds), HoMS not only buffers internal mechanical stress during charge/discharge cycles via dynamic stress-strain accommodation but also shortens ion diffusion pathways, enhances electron conductivity, and suppresses particle agglomeration. These effects collectively mitigate structural degradation, thereby boosting specific capacity, rate performance, and long-term cycling stability. For cathode materials (transition metal oxides, polyanionic compounds, and Prussian blue analogues), HoMS expands the electrode-electrolyte contact area, accelerates Na^+ intercalation/deintercalation kinetics, and inhibits transition metal ion dissolution and structural collapse. Notably, the tailored design of HoMS can be customized to target specific limitations of different electrode systems, enabling precise matching between structural advantages and material drawbacks, and achieving synergistic optimization of multiple performance metrics. These unique functions establish HoMS as a versatile platform tailored for SIBs rather than a universal strategy adapted directly from LIB research.

Nevertheless, it is worth noting that HoMS exhibits different suitability for SIB cathodes and anodes, with anodes being the optimal and more promising application scenario. The core structural advantages of HoMS, including volume buffering and a short ion transport pathway, are highly targeted to the key failure mechanisms of SIB anodes (e.g., severe volume expansion, sluggish Na^+ kinetics, and unstable SEI film). In contrast, the low tap density caused by the cavities of HoMS limits its application in SIB cathodes. In addition, it is worth noting that due to their different sodium storage mechanisms, volume variation behaviors, and intrinsic physicochemical properties, HoMS shows distinct prospects and challenges for different types of anode materials. For carbon-based anodes, HoMS mitigates mild volume expansion (10%–20%). For conversion-type anodes, HoMS relieves moderate-severe volume expansion (100%–300%). As for alloy-type anodes with ultrahigh capacity but extreme volume expansion (200%–420%), HoMS presents a particularly targeted solution by stabilizing the structural deformation and suppressing pulverization and SEI rupture.

Despite remarkable progress in HoMS-based SIB electrodes, critical challenges persist on the path to industrialization and large-scale application. First, current fabrication processes are plagued by high costs and poor scalability. Most synthetic routes rely on template-based methods, which involve intricate steps

(template synthesis, precursor coating, and etching) and often require expensive reagents or harsh conditions. Moreover, these processes face issues such as low yield and environmental concerns, hindering their translation to industrial production. Second, precise regulation of structural parameters remains challenging. While HoMS with diverse morphologies and compositions have been reported, the quantitative manipulation of key parameters lacks universal strategies, and the underlying structure-property relationships are not fully elucidated, especially the dynamic evolution of HoMS during long-term cycling and its correlation with electrochemical performance.

To address these challenges, future research should focus on three interconnected directions. First, develop green, low-cost, and scalable synthesis techniques. Priority should be given to template-free strategies that simplify processes, reduce reagent consumption, and improve yield. Additionally, exploring continuous production technologies will be crucial for bridging the lab-to-industry gap. Second, establish quantitative structure-property relationships through integrated experimental and theoretical approaches. Advanced in situ/operando characterization techniques combined with density functional theory calculations and machine learning can be employed to decode the dynamic structural evolution of HoMS during Na^+ storage, enabling predictive design of structural parameters for targeted performance. Third, expand the application scope of HoMS to the entire SIB system. Current research is primarily focused on electrodes, while the potential of HoMS in separators and electrolytes remains largely untapped. In separator engineering, the hierarchical porosity and large surface area of HoMS will facilitate sufficient electrolyte infiltration, accelerate Na^+ transport, and suppress the shuttling of polysulfides and transition-metal ions, thus reinforcing mechanical stability and stabilizing electrode/separator interfaces. As electrolyte additives, HoMS can serve as versatile carriers to promote the formation of stable SEI/CEI films, mitigate concentration polarization, and inhibit undesired electrolyte decomposition. These advantages endow HoMS with great promise for optimizing both separators and electrolytes toward high-performance SIBs. Therefore, exploring HoMS-based multi-component integration will facilitate the development of high-performance full-cell SIBs with balanced energy density, rate capability, and cycling life.

In conclusion, the structural design of HoMS provides a paradigm-shifting solution for overcoming the intrinsic limitations of SIB electrode materials. With the advancement of scalable synthesis, in-depth understanding of structure-property relationships, and expansion to multi-component applications, HoMS-based materials are poised to play a pivotal role in advancing SIB technology. This will not only accelerate the industrialization and commercialization of SIBs in large-scale energy storage but also offer valuable insights for the structural optimization of electrode materials in other electrochemical energy storage systems.

Funding

This work was supported by the National Natural Science Foundation of China (92572205, 52572247, 52372170, 52301296, W2512061 and 52261160573), the Scientific Foundation for Youth Scholars of Shenzhen University (868000001033528), the National Key Research and Development Program (2024YFA1509400, 2022YFA1504101 and 2022YFA1204502), the Shenzhen University 2035 Program for Excellent Research (2024B005), the Beijing Natural Science Foundation–Basic Research Cooperation Project of Beijing-Tianjin-Hebei Region (B2024204027), the Beijing Natural Science Foundation (Z230019), and the Institute of Process Engineering (IPE) Project for Frontier Basic Research (QYJC-2022-008).

Author contributions

R.Y. and J.W. conceptualized and coordinated the review. Z.S. wrote the whole draft of the review. R.Y., D.W., J.W. and N.W. helped to revise the review. All authors contributed to revisions and approved the final manuscript.

Conflict of interest

The authors declare no conflict of interest.

References

1 Weng J, Jossen A, Stefanopoulou A, *et al.* Fast-charging lithium-ion batteries require a systems engineering approach. *Nat Energy* 2025; **10**: 1289–1290.

2 Xu J, Cai X, Cai S, *et al.* High-energy lithium-ion batteries: Recent progress and a promising future in applications. *Energy Environ Mater* 2023; **6**: e12450.

3 Han L, Ling Y, Liu F, *et al.* Fiber-shaped aqueous battery: Design, advancements, and perspectives. *Natl Sci Open* 2025; **4**: 20250051.

4 Zhang Z, Chen Y, Sun S, *et al.* Recent progress on three-dimensional nanoarchitecture anode materials for lithium/sodium storage. *J Mater Sci Tech* 2022; **119**: 167–181.

5 Vaalma C, Buchholz D, Weil M, *et al.* A cost and resource analysis of sodium-ion batteries. *Nat Rev Mater* 2018; **3**: 18013.

6 Zhang F, He B, Xin Y, *et al.* Emerging chemistry for wide-temperature sodium-ion batteries. *Chem Rev* 2024; **124**: 4778–4821.

7 Zhao C, Lu Y, Li Y, *et al.* Novel methods for sodium-ion battery materials. *Small Methods* 2017; **1**: 1600063.

8 Bai Z, Yao Q, Wang M, *et al.* Low-temperature sodium-ion batteries: Challenges and progress. *Adv Energy Mater* 2024; **14**: 2303788.

9 Yang C, Xin S, Mai L, *et al.* Materials design for high-safety sodium-ion battery. *Adv Energy Mater* 2021; **11**: 2000974.

10 He H, Sun D, Tang Y, *et al.* Understanding and improving the initial Coulombic efficiency of high-capacity anode materials for practical sodium ion batteries. *Energy Storage Mater* 2019; **23**: 233–251.

11 Yang Y, Yang Y, Yang Y, *et al.* Advanced electrolyte engineering for low-temperature sodium-ion batteries. *Adv Mater* 2026; **38**: e13868.

12 Zhang Z, Wang R, Zeng J, *et al.* Size effects in sodium ion batteries. *Adv Funct Mater* 2021; **31**: 2106047.

13 Wang Z, Zhang H, Gao W, *et al.* Enabling ultrafast Na^+ diffusion kinetics via short-range-ordered and few-layered pitch-derived hard carbon towards high-rate sodium-ion batteries. *Energy Storage Mater* 2025; **83**: 104740.

14 Liang Y, Lai WH, Miao Z, *et al.* Nanocomposite materials for the sodium-ion battery: A review. *Small* 2018; **14**: 1702514.

15 Tsujimoto S, Lee C, Nunokawa R, *et al.* Kinetic insights into na ion transfer at the carbon-based negative electrode/electrolyte interfaces for sodium-ion batteries. *ChemElectroChem* 2024; **11**: e202400275.

16 Zhao C, Wang Q, Yao Z, *et al.* Rational design of layered oxide materials for sodium-ion batteries. *Science* 2020; **370**: 708–711.

17 Fang Y, Yu XY, Lou XWD. Nanostructured electrode materials for advanced sodium-ion batteries. *Matter* 2019; **1**: 90–114.

18 Hong F, Li Y, Zhou X, *et al.* Recent advances for medium- and high-entropy based layered cathodes for sodium ion batteries. *Nano Res Energy* 2025; **4**: e9120185.

19 Li W, Duan Y, Ge S, *et al.* Locking-chain electrolyte additive enabling moisture-tolerant electrolytes for sodium-ion batteries. *Nat Commun* 2025; **16**: 6405.

20 Yang M, Chang X, Wang L, *et al.* Interface modulation of metal sulfide anodes for long-cycle-life sodium-ion

batteries. *Adv Mater* 2023; **35**: 2208705.

21 Yang JL, Zhao XX, Zhang W, *et al.* "Pore-hopping" ion transport in cellulose-based separator towards high-performance sodium-ion batteries. *Angew Chem Int Ed* 2023; **62**: e202300258.

22 Li B, Liu Y, Han X, *et al.* Electrospun nanofiber surface-modified polyethylene separator for enhanced cycling stability and low-temperature performance of sodium-ion batteries. *Chem Eng J* 2024; **501**: 157803.

23 Mao D, Wang C, Li W, *et al.* Hollow multishelled structure: Synthesis chemistry and application. *Chem Res Chin Univ* 2024; **40**: 346–393.

24 Salhabi EHM, Zhao J, Wang J, *et al.* Hollow multi-shelled structural TiO_{2-x} with multiple spatial confinement for long-life lithium–sulfur batteries. *Angew Chem* 2019; **131**: 9176–9180.

25 Wei P, Wang H, Yang M, *et al.* Relocatable hollow multishelled structure-based membrane enables dendrite-free lithium deposition for ultrastable lithium metal batteries. *Adv Energy Mater* 2024; **14**: 2400108.

26 Rao F, Xiao Q, Wei Y, *et al.* Balanced polysulfide containment and lithium ion transport in lithium-sulfur batteries via nitrogen-doped carbon hollow multi-shelled structures on modified separators. *Chem Res Chin Univ* 2024; **40**: 690–698.

27 Li B, Wang J, Bi R, *et al.* Accurately localizing multiple nanoparticles in a multishelled matrix through shell-to-core evolution for maximizing energy-storage capability. *Adv Mater* 2022; **34**: 2200206.

28 Zhao X, Yang M, Wang J, *et al.* Hollow multishelled structural Li-rich cathode with Al doping enabling capacity and voltage stabled Li-ion batteries. *Chem Res Chin Univ* 2023; **39**: 630–635.

29 Zhao J, Wang J, Bi R, *et al.* General synthesis of multiple-cores@multiple-shells hollow composites and their application to lithium-ion batteries. *Angew Chem Int Ed* 2021; **60**: 25719–25722.

30 Wang H, Wei P, Wang J, *et al.* Hollow multishelled structure reviving lithium metal anode for high-energy-density batteries. *Chem Res Chin Univ* 2024; **40**: 428–436.

31 Xu S, Hessel CM, Ren H, *et al.* α-Fe_2O_3 multi-shelled hollow microspheres for lithium ion battery anodes with superior capacity and charge retention. *Energy Environ Sci* 2014; **7**: 632–637.

32 Ren H, Yu R, Wang J, *et al.* Multishelled TiO_2 hollow microspheres as anodes with superior reversible capacity for lithium ion batteries. *Nano Lett* 2014; **14**: 6679–6684.

33 Wang J, Tang H, Zhang L, *et al.* Multi-shelled metal oxides prepared via an anion-adsorption mechanism for lithium-ion batteries. *Nat Energy* 2016; **1**: 16050.

34 Cai X, Yue Y, Yi Z, *et al.* Challenges and industrial perspectives on the development of sodium ion batteries. *Nano Energy* 2024; **129**: 110052.

35 Yabuuchi N, Kubota K, Dahbi M, *et al.* Research development on sodium-ion batteries. *Chem Rev* 2014; **114**: 11636–11682.

36 Hwang JY, Myung ST, Sun YK. Sodium-ion batteries: Present and future. *Chem Soc Rev* 2017; **46**: 3529–3614.

37 Chen Y, Zhao B, Yang Y, *et al.* Toward high-areal-capacity electrodes for lithium and sodium ion batteries. *Adv Energy Mater* 2022; **12**: 2201834.

38 Yang F, Gao H, Chen J, *et al.* Phosphorus-based materials as the anode for sodium-ion batteries. *Small Methods* 2017; **1**: 1700216.

39 Song J, Xiao B, Lin Y, *et al.* Interphases in sodium-ion batteries. *Adv Energy Mater* 2018; **8**: 1703082.

40 Li H, Xu M, Zhang Z, *et al.* Engineering of polyanion type cathode materials for sodium-ion batteries: Toward higher energy/power density. *Adv Funct Mater* 2020; **30**: 2000473.

41 Lv Z, Li T, Hou X, *et al.* Solvation structure and solid electrolyte interface engineering for excellent Na^+ storage performances of hard carbon with the ether-based electrolytes. *Chem Eng J* 2022; **430**: 133143.

42 Qin N, Sun Y, Hu C, *et al.* Boosting high initial coulombic efficiency of hard carbon by *in-situ* electrochemical presodiation. *J Energy Chem* 2023; **77**: 310–316.

43 Yang Y, Wu C, He XX, *et al.* Boosting the development of hard carbon for sodium-ion batteries: Strategies to optimize the initial coulombic efficiency. *Adv Funct Mater* 2024; **34**: 2302277.

44 Li Y, Vasileiadis A, Zhou Q, *et al.* Origin of fast charging in hard carbon anodes. *Nat Energy* 2024; **9**: 134–142.

45 Wang J, Wan J, Wang D. Hollow multishelled structures for promising applications: Understanding the structure–performance correlation. *Acc Chem Res* 2019; **52**: 2169–2178.

46 Wang L, Wan J, Wang J, *et al.* Small structures bring big things: Performance control of hollow multishelled structures. *Small Struct* 2021; **2**: 2000041.

47 Yu L, Hu H, Wu HB, *et al.* Complex hollow nanostructures: Synthesis and energy-related applications. *Adv Mater* 2017; **29**: 1604563.

48 Cui Y, Zhang L, Huo Q, *et al.* Construction of hollow porous double-shell NSC@WS_2 nanospheres for improved sodium-ion battery performance. *J Energy Storage* 2025; **113**: 115688.

49 Ma M, Yao Y, Wu Y, *et al.* Progress and prospects of transition metal sulfides for sodium storage. *Adv Fiber Mater* 2020; **2**: 314–337.

50 Li L, Zheng Y, Zhang S, *et al.* Recent progress on sodium ion batteries: Potential high-performance anodes. *Energy Environ Sci* 2018; **11**: 2310–2340.

51 Zhao R, Sun N, Xu B. Recent advances in heterostructured carbon materials as anodes for sodium-ion batteries. *Small Struct* 2021; **2**: 2100132.

52 Zhou L, Cui Y, Niu P, *et al.* Biomass-derived hard carbon material for high-capacity sodium-ion battery anode through structure regulation. *Carbon* 2025; **231**: 119733.

53 Wang H, Chen H, Chen C, *et al.* Tea-derived carbon materials as anode for high-performance sodium ion batteries. *Chin Chem Lett* 2023; **34**: 107465.

54 Hu Z, Chen Z, Liu Q, *et al.* Compact TiO_2@SnO_2@C heterostructured particles as anode materials for sodium-ion batteries with improved volumetric capacity. *iScience* 2023; **26**: 106642.

55 Jing WT, Yang CC, Jiang Q. Recent progress on metallic Sn- and Sb-based anodes for sodium-ion batteries. *J Mater Chem A* 2020; **8**: 2913–2933.

56 Qu B, Ma C, Ji G, *et al.* Layered SnS_2-reduced graphene oxide composite—A high-capacity, high-rate, and long-cycle life sodium-ion battery anode material. *Adv Mater* 2014; **26**: 3854–3859.

57 Wang D, Ma Q, He H, *et al.* Double-confined nanoheterostructure Sb/Sb_2S_3@$Ti_3C_2T_x$@C toward ultra-stable Li-/Na-ion batteries. *Rare Met* 2024; **43**: 2067–2079.

58 Bhar M, Ghosh S, Martha SK. Designing freestanding electrodes with Fe_2O_3-based conversion type anode material for sodium-ion batteries. *J Alloys Compd* 2023; **948**: 169670.

59 Jiang L, Dou Y, Song W, *et al.* Heterointerface magic: How FeS_2/NiS_2@NC nanoparticles transform sodium-ion battery anode performance. *J Colloid Interface Sci* 2025; **686**: 589–598.

60 Hong QJ, Subramani M, Hsieh CM, *et al.* First-principles investigation of FeP@Graphene as anode material for sodium-ion batteries. *Appl Surf Sci* 2026; **719**: 165131.

61 Zhang L, Zhu B, Xu D, *et al.* Yolk-shell $FeSe_2$@$CoSe_2$/$FeSe_2$ heterojunction as anode materials for sodium-ion batteries with high rate capability and stability. *J Mater Sci Tech* 2024; **172**: 185–195.

62 Babu SK, Wu PJ, Liu WR. MOF-derived spinel $NiCo_2O_4$ anchored single-walled carbon nanotubes nanocomposite as potential anode materials for Na-ion batteries. *Electrochim Acta* 2025; **535**: 146600.

63 Wan F, Wu XL, Guo JZ, *et al.* Nanoeffects promote the electrochemical properties of organic $Na_2C_8H_4O_4$ as anode material for sodium-ion batteries. *Nano Energy* 2015; **13**: 450–457.

64 Wu X, Ma J, Ma Q, *et al.* A spray drying approach for the synthesis of a $Na_2C_6H_2O_4$/CNT nanocomposite anode for sodium-ion batteries. *J Mater Chem A* 2015; **3**: 13193–13197.

65 Liu J, You Y, Huang L, *et al.* Precisely tunable instantaneous carbon rearrangement enables low-working-potential hard carbon toward sodium-ion batteries with enhanced energy density. *Adv Mater* 2024; **36**: 2407369.

66 Yin Y, Tan Y, Lu Y, *et al.* A soft carbon/hard carbon composite synthesized from asphalt/pecan shells as an anode material for sodium-ion batteries. *J Energy Storage* 2025; **113**: 115649.

67 Sun J, Lee HW, Pasta M, *et al.* A phosphorene–graphene hybrid material as a high-capacity anode for sodium-ion

batteries. *Nat Nanotech* 2015; **10**: 980–985.

68 An J, Wang F, Yang JY, *et al.* An ion-pumping interphase on graphdiyne/graphite heterojunction for fast-charging lithium-ion batteries. *CCS Chem* 2024; **6**: 110–124.

69 Wang F, Jiang Z, Zhang Y, *et al.* Revitalizing sodium-ion batteries via controllable microstructures and advanced electrolytes for hard carbon. *eScience* 2024; **4**: 100181.

70 Fang H, Wei X, Hu W, *et al.* Regulating interfacial chemistry of hard carbon anodes by *in situ* coupling strategy for high-rate sodium-ion batteries. *eSci Energy* 2025; **1**: 100001.

71 Ma Y, Cheng Y, Dang Z, *et al.* The tune of shell numbers of multi-shell hollow mesoporous carbon microspheres for enhanced microwave absorption. *Carbon* 2024; **227**: 119267.

72 Bin DS, Li Y, Sun YG, *et al.* Structural engineering of multishelled hollow carbon nanostructures for high-performance Na-ion battery anode. *Adv Energy Mater* 2018; **8**: 1800855.

73 Bu L, Kuai X, Zhu W, *et al.* Nitrogen-doped double-shell hollow carbon spheres for fast and stable sodium ion storage. *Electrochim Acta* 2020; **356**: 136804.

74 Zhang K, Li X, Liang J, *et al.* Nitrogen-doped porous interconnected double-shelled hollow carbon spheres with high capacity for lithium ion batteries and sodium ion batteries. *Electrochim Acta* 2015; **155**: 174–182.

75 Yu M, Sun M, Zhu L, *et al.* Double-shell and hierarchical porous nitrogen-doped carbon nanocages as superior anode material for advanced sodium-ion batteries. *J Energy Storage* 2024; **86**: 111211.

76 Chattopadhyay S, Pramanik A, Pieshkov T, *et al.* B, N Co-doped hard carbon nano-sponge enhancing half and full cell performance in Na-ion batteries. *Small* 2025; **21**: 2500120.

77 Ma X, Hu J, Zhang W, *et al.* An effective B-doped strategy to regulate the closed-pore formation of hard carbon nanospheres for sodium-ion batteries. *J Energy Storage* 2025; **126**: 117149.

78 Jin Q, Wang K, Feng P, *et al.* Surface-dominated storage of heteroatoms-doping hard carbon for sodium-ion batteries. *Energy Storage Mater* 2020; **27**: 43–50.

79 Hong Z, Zhen Y, Ruan Y, *et al.* Rational design and general synthesis of S-doped hard carbon with tunable doping sites toward excellent Na-ion storage performance. *Adv Mater* 2018; **30**: 1802035.

80 Liu ZG, Zhao J, Yao H, *et al.* P-doped spherical hard carbon with high initial coulombic efficiency and enhanced capacity for sodium ion batteries. *Chem Sci* 2024; **15**: 8478–8487.

81 Wang Y, Wang Y, Zhang L, *et al.* Exogenous phosphorus supplementation and sodium reduction treatment to realize N, P co-doped hard carbon with reduced oxygen-containing groups for high-performance sodium-ion batteries. *J Power Sources* 2025; **630**: 236156.

82 Liu L, Gui L, Hu R, *et al.* Bi-doped commercial hard carbon with enhanced slope capacity to deliver superior rate performance for sodium-ion batteries. *ACS Appl Energy Mater* 2025; **8**: 4211–4219.

83 Lu Z, Wang J, Feng W, *et al.* Zinc single-atom-regulated hard carbons for high-rate and low-temperature sodium-ion batteries. *Adv Mater* 2023; **35**: 2211461.

84 Edison E, Sreejith S, Ren H, *et al.* Microstructurally engineered nanocrystalline Fe–Sn–Sb anodes: Towards stable high energy density sodium-ion batteries. *J Mater Chem A* 2019; **7**: 14145–14152.

85 Zheng SM, Tian YR, Liu YX, *et al.* Alloy anodes for sodium-ion batteries. *Rare Met* 2021; **40**: 272–289.

86 Wang X, Zhao X, Wang L. Bulk alloy anodes for sodium-ion batteries. *Batteries Supercaps* 2025; **8**: e202400551.

87 Lao M, Zhang Y, Luo W, *et al.* Alloy-based anode materials toward advanced sodium-ion batteries. *Adv Mater* 2017; **29**: 1700622.

88 Song K, Liu C, Mi L, *et al.* Recent progress on the alloy-based anode for sodium-ion batteries and potassium-ion batteries. *Small* 2021; **17**: 1903194.

89 Tan H, Chen D, Rui X, *et al.* Peering into alloy anodes for sodium-ion batteries: Current trends, challenges, and opportunities. *Adv Funct Mater* 2019; **29**: 1808745.

90 Li Y, Mei Y, Liu H, *et al.* Functional carbon dots induced defect configuration entropy strengthening polyanion cathode for ultrafast-charging sodium ion batteries in a wide temperature. *Nano Energy* 2024; **130**: 110107.

91 He S, Wu H, Li S, *et al.* Small but mighty: Empowering sodium/potassium-ion battery performance with S-doped SnO_2 quantum dots embedded in N, S codoped carbon fiber network. *Carbon Energy* 2024; **6**: e486.

92 Wang YX, Yang J, Chou SL, *et al.* Uniform yolk-shell iron sulfide–carbon nanospheres for superior sodium–iron sulfide batteries. *Nat Commun* 2015; **6**: 8689.

93 Wang JW, Liu XH, Mao SX, *et al.* Microstructural evolution of tin nanoparticles during *in situ* sodium insertion and extraction. *Nano Lett* 2012; **12**: 5897–5902.

94 Wu X, Wu H, Xie B, *et al.* Atomic welded dual-wall hollow nanospheres for three-in-one hybrid storage mechanism of alkali metal ion batteries. *ACS Nano* 2021; **15**: 14125–14136.

95 He J, Wei Y, Zhai T, *et al.* Antimony-based materials as promising anodes for rechargeable lithium-ion and sodium-ion batteries. *Mater Chem Front* 2018; **2**: 437–455.

96 Su J, Li W, Duan T, *et al.* Graphene/antimonene/graphene heterostructure: A potential anode for sodium-ion batteries. *Carbon* 2019; **153**: 767–775.

97 Liu Y, Qing Y, Zhou B, *et al.* Yolk–shell Sb@void@graphdiyne nanoboxes for high-rate and long cycle life sodium-ion batteries. *ACS Nano* 2023; **17**: 2431–2439.

98 Kong M, Liu Y, Zhou B, *et al.* Rational design of Sb@C@TiO_2 triple-shell nanoboxes for high-performance sodium-ion batteries. *Small* 2020; **16**: 2001976.

99 Sang J, Liu K, Zhang X, *et al.* Enabling high-performance sodium battery anodes by complete reduction of graphene oxide and cooperative *in-situ* crystallization of ultrafine SnO_2 nanocrystals. *Energy Environ Mater* 2023; **6**: e12431.

100 Cui Z, He SA, Zhu J, *et al.* Tailoring the void space using nanoreactors on carbon fibers to confine SnS_2 nanosheets for ultrastable lithium/sodium-ion batteries. *Small Methods* 2022; **6**: 2101484.

101 Zheng Y, Liu C, Zhang Z, *et al.* Regulating (010) exposed facets of a Sb_2O_3 anode to achieve high-performance sodium-ion batteries. *Nano Lett* 2025; **25**: 5461–5468.

102 Xie J, Liu L, Xia J, *et al.* Template-free synthesis of Sb_2S_3 hollow microspheres as anode materials for lithium-ion and sodium-ion batteries. *Nano-Micro Lett* 2018; **10**: 12.

103 Liu Z, Wang X, Wu Z, *et al.* Ultrafine Sn_4P_3 nanocrystals from chloride reduction on mechanically activated Na surface for sodium/lithium ion batteries. *Nano Res* 2020; **13**: 3157–3164.

104 Xie B, Wu X, Wang JH, *et al.* Confinement sacrifice template synthesis of size controllable heterogeneous double-layer hollow spheres SnO_2@Void@HCSs as anode for Li^+/Na^+ batteries. *J Electroanal Chem* 2022; **923**: 116830.

105 Huang S, Meng C, Xiao M, *et al.* Multi-shell tin phosphide nanospheres as high performance anode material for a sodium ion battery. *Sustain Energy Fuels* 2017; **1**: 1944–1949.

106 Choi SH, Kang YC. Synergetic effect of yolk–shell structure and uniform mixing of SnS–MoS_2 nanocrystals for improved Na-ion storage capabilities. *ACS Appl Mater Interfaces* 2015; **7**: 24694–24702.

107 Xie F, Zhang L, Gu Q, *et al.* Multi-shell hollow structured Sb_2S_3 for sodium-ion batteries with enhanced energy density. *Nano Energy* 2019; **60**: 591–599.

108 Zhang Y, Lim YV, Huang S, *et al.* Tailoring NiO nanostructured arrays by sulfate anions for sodium-ion batteries. *Small* 2018; **14**: 1800898.

109 Liu Y, Lin Q, Chen X, *et al.* Fe_3O_4/Fe/FeS tri-heterojunction node spawning N-carbon nanotube scaffold structure for high-performance sodium-ion battery. *Energy Environ Mater* 2024; **7**: e12684.

110 Zhao W, Zhou Y, Zhou H, *et al.* Optimizing reversible phase-transformation of FeS_2 anode via atomic-interface engineering toward fast-charging sodium storage: Theoretical predication and experimental validation. *Adv Sci* 2025; **12**: 2411884.

111 Wu H, Xia G, Yu X. Unlocking the potential of iron sulfides for sodium-ion batteries by ultrafine pulverization. *Small* 2024; **20**: 2312190.

112 Liang J, Sun J, Cao X, *et al.* Enhanced reaction kinetics in sodium-ion batteries achieved by 3D heterostructure CoS_2/CoS with self-induced internal electric field. *Adv Sci* 2025; **12**: 2502241.

113 Zhang X, Wang J, Hou W, *et al.* Prussian blue analogues-derived highly stable and conductive $CoSe_2$/$FeSe_2$@C

composite anode for sodium-ion batteries. *J Energy Storage* 2025; **138**: 118701.

114 Pan Q, Zhang M, Zhang L, *et al.* $FeSe_2$@C microrods as a superior long-life and high-rate anode for sodium ion batteries. *ACS Nano* 2020; **14**: 17683–17692.

115 Ihsan-Ul-Haq M, Huang H, Cui J, *et al.* Chemical interactions between red P and functional groups in NiP_3/CNT composite anodes for enhanced sodium storage. *J Mater Chem A* 2018; **6**: 20184–20194.

116 Xia J, Guo J, Li S, *et al.* Progress of FeP anode materials for alkali metal ion batteries. *RSC Adv* 2025; **15**: 10395–10418.

117 Xia H, Li Z, Ma J, *et al.* Developments and prospects of conversion reaction-based anode materials in sodium-ion batteries. *Chem Commun* 2025; **61**: 18987–19003.

118 Puthusseri D, Wahid M, Ogale S. Conversion-type anode materials for alkali-ion batteries: State of the art and possible research directions. *ACS Omega* 2018; **3**: 4591–4601.

119 Qi S, Mi L, Song K, *et al.* Understanding shuttling effect in sodium ion batteries for the solution of capacity fading: FeS_2 as an example. *J Phys Chem C* 2019; **123**: 2775–2782.

120 Wu C, Dou SX, Yu Y. The state and challenges of anode materials based on conversion reactions for sodium storage. *Small* 2018; **14**: 1703671.

121 Chen S, Ye S, Xu X, *et al.* Recent advances in conversion-type iron-based materials for sodium-ion batteries. *Microstructures* 2025; **5**: 2025084.

122 Xu H, Li H, Wang X. The anode materials for lithium-ion and sodium-ion batteries based on conversion reactions: A review. *ChemElectroChem* 2023; **10**: e202201151.

123 Alcántara R, Jaraba M, Lavela P, *et al.* $NiCo_2O_4$ spinel: First report on a transition metal oxide for the negative electrode of sodium-ion batteries. *Chem Mater* 2002; **14**: 2847–2848.

124 Zhu C, Xu F, Min H, *et al.* Identifying the conversion mechanism of $NiCo_2O_4$ during sodiation–desodiation cycling by *in situ* TEM. *Adv Funct Mater* 2017; **27**: 1606163.

125 Zhang Y, Xiao X, Zhang W, *et al.* Facile formation of $NiCo_2O_4$ yolk-shell spheres for highly reversible sodium storage. *J Alloys Compd* 2019; **800**: 125–133.

126 Zhang X, Zhou Y, Luo B, *et al.* Microwave-assisted synthesis of $NiCo_2O_4$ double-shelled hollow spheres for high-performance sodium ion batteries. *Nano-Micro Lett* 2018; **10**: 13.

127 Li Y, Zhang S, Wang S, *et al.* A multi-shelled V_2O_3/C composite with an overall coupled carbon scaffold enabling ultrafast and stable lithium/sodium storage. *J Mater Chem A* 2019; **7**: 19234–19240.

128 Wei Y, Cheng Y, Zhao D, *et al.* A universal formation mechanism of hollow multi-shelled structures dominated by concentration waves. *Angew Chem Int Ed* 2023; **62**: e202302621.

129 Zhang X, Bi R, Wang J, *et al.* Delicate Co-control of shell structure and sulfur vacancies in interlayer-expanded tungsten disulfide hollow sphere for fast and stable sodium storage. *Adv Mater* 2023; **35**: 2209354.

130 Wang H, Chen S, Fu C, *et al.* Recent advances in conversion-type electrode materials for post lithium-ion batteries. *ACS Mater Lett* 2021; **3**: 956–977.

131 Wang X, Chen Y, Fang Y, *et al.* Synthesis of cobalt sulfide multi-shelled nanoboxes with precisely controlled two to five shells for sodium-ion batteries. *Angew Chem Int Ed* 2019; **58**: 2675–2679.

132 Fang Y, Guan BY, Luan D, *et al.* Synthesis of CuS@CoS_2 double-shelled nanoboxes with enhanced sodium storage properties. *Angew Chem Int Ed* 2019; **58**: 7739–7743.

133 Li X, Xiang Y, Deng R, *et al.* Metal organic frameworks-derived multi-shell copper-cobalt-zinc sulfide cubes for sodium-ion battery anode. *Chem Eng J* 2021; **425**: 131501.

134 Chen M, Gu S, Li J, *et al.* Triple-shell hollow FeS/MoS_2 heterostructure anodes: Synergistic effects of built-in electric field on ultra-stable sodium storage. *Adv Sci* 2025; **12**: e09997.

135 Chen M, Liu Y, Fang Z, *et al.* High-entropy sulfide nanoarchitectures with triple-shelled hollow design for durable sodium–ion batteries. *Nanomaterials* 2025; **15**: 881.

136 Hou P, Dong M, Li F, *et al.* Recent advances in cathode materials with core–shell structures and concentration

gradients for advanced sodium-ion batteries. *Adv Funct Mater* 2024; **34**: 2409518.

137 Wu J, Tian J, Sun X, *et al.* Cycling performance of layered oxide cathode materials for sodium-ion batteries. *Int J Miner Metall Mater* 2024; **31**: 1720–1744.

138 Xu XQ, Chen JY, Jiang Y, *et al.* Origins of high air sensitivity and treatment strategies in O3-type $NaMn_{1/3}Fe_{1/3}Ni_{1/3}O_2$. *J Am Chem Soc* 2024; **146**: 22374–22386.

139 Huang J, Li W, Ye D, *et al.* Designing ultrastable P2/O3-type layered oxides for sodium ion batteries by regulating Na distribution and oxygen redox chemistry. *J Energy Chem* 2024; **94**: 466–476.

140 Zhang S, Zhou T, Pan Y, *et al.* Constructing built-in electric field in $Na_3V_2(PO_4)_3/NaV(P_2O_7)$ heterostructure with columnar cluster morphology boosting high capacity and energy density for sodium ion batteries. *Adv Funct Mater* 2026; **36**: e14171.

141 Sun H, Jiang Y, Dai H, *et al.* Upcycling iron sulfate waste into low-cost and high-stability $Na_2Fe(SO_4)_2$ cathode materials for sodium-ion batteries. *ACS Sustain Chem Eng* 2025; **13**: 15141–15148.

142 Cai Y, Cheng H, Chen Z, *et al.* The interface interaction of sulfur-doped carbon boosting kinetics of $Na_4Fe_3(PO_4)_2(P_2O_7)$ for high rate and stable sodium-ion batteries. *Sci China Mater* 2025; **68**: 3675–3684.

143 Yang L, Liu Q, Wan M, *et al.* Surface passivation of $Na_xFe[Fe(CN)_6]$ cathode to improve its electrochemical kinetics and stability in sodium-ion batteries. *J Power Sources* 2020; **448**: 227421.

144 Tang Y, Wang L, Hu J, *et al.* Epitaxial Nucleation of $Na_xFeFe(CN)_6$@rGO with improved lattice regularity as ultrahigh-rate cathode for sodium-ion batteries. *Adv Energy Mater* 2024; **14**: 2303015.

145 Liu S, Yu H, Zhao Y, *et al.* Inhibiting phase transitions of prussian blue analogs with high-entropy strategy for ultralong-life sodium-ion battery cathodes. *Small* 2025; **21**: 2504893.

146 Jiang M, Zhao Y, Hou Z, *et al.* leveraging sodium storage of water-deficient prussian blue analogues by deep eutectic chemistry. *ACS Energy Lett* 2026; **11**: 526–536.

147 Jing Z, Kong L, Mamoor M, *et al.* Rational design of prussian blue analogues for ultralong and wide-temperature-range sodium-ion batteries. *J Am Chem Soc* 2025; **147**: 3702–3713.

148 Yang H, Wang D, Liu Y, *et al.* Improvement of cycle life for layered oxide cathodes in sodium-ion batteries. *Energy Environ Sci* 2024; **17**: 1756–1780.

149 Lu X, Li S, Li Y, *et al.* From lab to application: Challenges and opportunities in achieving fast charging with polyanionic cathodes for sodium-ion batteries. *Adv Mater* 2024; **36**: 2407359.

150 Ge L, Song Y, Niu P, *et al.* Elaborating the crystal water of prussian blue for outstanding performance of sodium ion batteries. *ACS Nano* 2024; **18**: 3542–3552.

151 Xiang X, Zhang K, Chen J. Recent advances and prospects of cathode materials for sodium-ion batteries. *Adv Mater* 2015; **27**: 5343–5364.

152 Liu XY, Li S, Zhu YF, *et al.* Promoting layered oxide cathodes based on structural reconstruction for sodium-ion batteries: Reversible phase transition, stable interface regulation, and multifunctional intergrowth structure. *Adv Funct Mater* 2025; **35**: 2414130.

153 Guo YJ, Jin RX, Fan M, *et al.* Sodium layered oxide cathodes: Properties, practicality and prospects. *Chem Soc Rev* 2024; **53**: 7828–7874.

154 Wang J, Zhu YF, Su Y, *et al.* Routes to high-performance layered oxide cathodes for sodium-ion batteries. *Chem Soc Rev* 2024; **53**: 4230–4301.

155 Zhang K, Kim D, Hu Z, *et al.* Manganese based layered oxides with modulated electronic and thermodynamic properties for sodium ion batteries. *Nat Commun* 2019; **10**: 5203.

156 Lu D, Yao Z, Zhong Y, *et al.* Polypyrrole-coated sodium manganate hollow microspheres as a superior cathode for sodium ion batteries. *ACS Appl Mater Interfaces* 2019; **11**: 15630–15637.

157 Zhao X, Wang J, Yu R, *et al.* Construction of multishelled binary metal oxides via coabsorption of positive and negative ions as a superior cathode for sodium-ion batteries. *J Am Chem Soc* 2018; **140**: 17114–17119.

158 Jin T, Li H, Zhu K, *et al.* Polyanion-type cathode materials for sodium-ion batteries. *Chem Soc Rev* 2020; **49**: 2342–

2377.

159 Niu Y, Zhao Y, Xu M. Manganese-based polyanionic cathodes for sodium-ion batteries. *Carbon Neutralization* 2023; **2**: 150–168.

160 Guo D, Chu S, Zhang B, *et al.* The development and prospect of stable polyanion compound cathodes in LIBs and promising complementers. *Small Methods* 2024; **8**: 2400587.

161 Ni Q, Bai Y, Wu F, *et al.* Polyanion-type electrode materials for sodium-ion batteries. *Adv Sci* 2017; **4**: 1600275.

162 Zhao L, Rong X, Niu Y, *et al.* Ostwald ripening tailoring hierarchically porous $Na_3V_2(PO_4)_2O_2F$ hollow nanospheres for superior high-rate and ultrastable sodium ion storage. *Small* 2020; **16**: 2004925.

163 Fu Q, Song F, Mu C, *et al.* Activating reversible multi-electron reaction of $Na_3(VO)_2(PO_4)_2F$ cathode via Fe/F dual-doping for high-energy and stable sodium storage. *Energy Storage Mater* 2025; **74**: 103960.

164 Qi Y, Tong Z, Zhao J, *et al.* Scalable room-temperature synthesis of multi-shelled $Na_3(VOPO_4)_2F$ microsphere cathodes. *Joule* 2018; **2**: 2348–2363.

165 Yin Y, Pei C, Xiong F, *et al.* Porous yolk-shell structured $Na_3(VO)_2(PO_4)_2F$ microspheres with enhanced Na-ion storage properties. *J Mater Sci Tech* 2021; **83**: 83–89.

166 Wang X, Li H, Zhang W, *et al.* Unlocking fast and highly reversible sodium storage in Fe-based mixed polyanion cathodes for low-cost and high-performance sodium-ion batteries. *J Mater Chem A* 2023; **11**: 6978–6985.

167 Ellis BL, Makahnouk WRM, Rowan-Weetaluktuk WN, *et al.* Crystal structure and electrochemical properties of A_2MPO_4F fluorophosphates (A = Na, Li; M = Fe, Mn, Co, Ni). *Chem Mater* 2010; **22**: 1059–1070.

168 Ling R, Cai S, Xie D, *et al.* Double-shelled hollow Na_2FePO_4F/C spheres cathode for high-performance sodium-ion batteries. *J Mater Sci* 2018; **53**: 2735–2747.

169 Hassan M, Zhao Y, Liu Q, *et al.* Progress on Fe-based cathode materials for sodium-ion batteries. *Carbon Neutraliz* 2025; **4**: e70000.

170 Xia Q, Zhang L, Wang D, *et al.* Metal ion complexation mediated synthesis of $Na_4Fe_3(PO_4)_2P_2O_7$/C hollow microspheres: Insights into structural evolution for high-performance sodium storage. *Energy Storage Mater* 2026; **84**: 104849.

171 Ma X, Pan Z, Wu X, *et al.* $Na_4Fe_3(PO_4)_2(P_2O_7)$@$NaFePO_4$@C core-double-shell architectures on carbon cloth: A high-rate, ultrastable, and flexible cathode for sodium ion batteries. *Chem Eng J* 2019; **365**: 132–141.

172 Qi X, Dong H, Yan H, *et al.* Hollow Core-Shelled $Na_4Fe_{2.4}Ni_{0.6}(PO_4)_2P_2O_7$ with tiny-void space capable fast-charge and low-temperature sodium storage. *Angew Chem Int Ed* 2024; **63**: e202410590.

173 Wu X, Wu C, Wei C, *et al.* Highly crystallized $Na_2CoFe(CN)_6$ with suppressed lattice defects as superior cathode material for sodium-ion batteries. *ACS Appl Mater Interfaces* 2016; **8**: 5393–5399.

174 Yang D, Xu J, Liao XZ, *et al.* Structure optimization of Prussian blue analogue cathode materials for advanced sodium ion batteries. *Chem Commun* 2014; **50**: 13377–13380.

175 Fan S, Liu Y, Gao Y, *et al.* The design and synthesis of Prussian blue analogs as a sustainable cathode for sodium-ion batteries. *SusMat* 2023; **3**: 749–780.

176 Wang W, Gang Y, Peng J, *et al.* Effect of eliminating water in prussian blue cathode for sodium-ion batteries. *Adv Funct Mater* 2022; **32**: 2111727.

177 Peng J, Huang J, Gao Y, *et al.* Defect-healing induced monoclinic iron-based prussian blue analogs as high-performance cathode materials for sodium-ion batteries. *Small* 2023; **19**: 2300435.

178 Qu Z, Luo W, Gao C, *et al.* Cryo-synthesized Prussian blue analogues as advanced cathode materials for potassium-ion batteries. *Natl Sci Open* 2025; **4**: 20250022.

179 Xie B, Zuo P, Wang L, *et al.* Achieving long-life Prussian blue analogue cathode for Na-ion batteries via triple-cation lattice substitution and coordinated water capture. *Nano Energy* 2019; **61**: 201–210.

180 Xu X, Zhu S, Yang C, *et al.* A novel strategy for the reduction of coordinated water in Prussian blue analogues for their application as cathode materials for sodium-ion batteries. *J Mater Chem A* 2025; **13**: 11848–11860.

181 Duan J, Sun Y, Li B, *et al.* Tailoring coordinated water in sodium-rich phase for high-performance Prussian blue

cathodes. *Nanoscale* 2025; **17**: 24707–24714.

182 Jang J, Jeong H, Hong J, *et al.* Anion effects on crystal water reactivity and cathode-electrolyte interphase of prussian blue in sodium-ion batteries. *Small Methods* 2026; **10**: 2500827.

183 Peng J, Zhang W, Liu Q, *et al.* Prussian blue analogues for sodium-ion batteries: Past, present, and future. *Adv Mater* 2022; **34**: 2108384.

184 Ding X, Zhou Q, Wang Z, *et al.* An ultra-stable Mn-based Prussian blue compound effectively suppresses Jahn–Teller distortion as a superior cathode material for sodium-ion batteries. *J Mater Chem A* 2024; **12**: 27598–27609.

185 Shang Y, Li X, Song J, *et al.* Unconventional Mn vacancies in Mn–Fe prussian blue analogs: Suppressing Jahn–Teller distortion for ultrastable sodium storage. *Chem* 2020; **6**: 1804–1818.

186 Wang Y, Yang C, Yao L, *et al.* Dissolution inhibition strategy stabilizes manganese prussian blue analogs for high-energy sodium-ion batteries. *Adv Funct Mater* 2025; **35**: 2423867.

187 Ji M, Jin T, Xu Q, *et al.* High-entropy layer grown on Mn-based prussian blue analog for na-ion storage. *ACS Energy Lett* 2025; **10**: 5165–5173.

188 Wang M, Ling R, Zhou C, *et al.* Sequentially epitaxial multi-shelled Mn-based Prussian blue cathode for highly stable sodium-ions batteries. *Energy Storage Mater* 2024; **69**: 103376.

189 Huang Y, Xie M, Wang Z, *et al.* A chemical precipitation method preparing hollow–core–shell heterostructures based on the prussian blue analogs as cathode for sodium-ion batteries. *Small* 2018; **14**: 1801246.

190 Wang CC, Zhang LL, Fu XY, *et al.* Hollow layered iron-based prussian blue cathode with reduced defects for high-performance sodium-ion batteries. *ACS Appl Mater Interfaces* 2024; **16**: 18959–18970.

191 Wan P, Xie H, Zhang N, *et al.* Stepwise hollow prussian blue nanoframes/carbon nanotubes composite film as ultrahigh rate sodium ion cathode. *Adv Funct Mater* 2020; **30**: 2002624.

192 Wei Y, Zheng M, Zhu W, *et al.* Hollow structures Prussian blue, its analogs, and their derivatives: Synthesis and electrochemical energy-related applications. *Carbon Neutraliz* 2023; **2**: 271–299.

193 Nai J, Zhang J, Lou XWD. Construction of single-crystalline prussian blue analog hollow nanostructures with tailorable topologies. *Chem* 2018; **4**: 1967–1982.

194 Nai J, Lou XWD. Hollow structures based on prussian blue and its analogs for electrochemical energy storage and conversion. *Adv Mater* 2019; **31**: 1706825.

195 Zhu X, Tang J, Huang H, *et al.* Hollow structured cathode materials for rechargeable batteries. *Sci Bull* 2020; **65**: 496–512.